Impact of Flight Enthalpy, Fuel Simulant, and Chemical Reactions on the Mixing Characteristics of Several Injectors at Hypervelocity Flow Conditions

Tomasz G. Drozda, Robert A. Baurle, and J. Philip Drummond
NASA Langley Research Center, Hampton, VA 23681

ABSTRACT

The high total temperatures or total enthalpies required to duplicate the high-speed flight conditions in ground experiments often place stringent requirements on the material selection and cooling needs for the test articles and intrusive flow diagnostic equipment. Furthermore, for internal flows, these conditions often complicate the use of nonintrusive diagnostics that need optical access to the test section and interior portions of the flowpath. Because of the technical challenges and increased costs associated with experimentation at high values of total enthalpy, an attempt is often made to reduce it. This is the case for the Enhanced Injection and Mixing Project (EIMP) currently underway in the Arc-Heated Scramjet Test Facility at the NASA Langley Research Center. The EIMP aims to investigate supersonic combustion ramjet (scramjet) fuel injection and mixing physics, improve the understanding of underlying physical processes, and develop enhancement strategies and functional relationships between mixing performance and losses relevant to flight Mach numbers greater than 8. The experiments will consider a "direct-connect" approach and utilize a Mach 6 nozzle to simulate the combustor entrance flow of a scramjet engine. However, while the value of the Mach number is matched to that expected at the combustor entrance in flight, the maximum value of the total enthalpy for these experiments is limited by the thermal-structural limits of the uncooled experimental hardware. Furthermore, the fuel simulant is helium, not hydrogen. The use of "cold" flows and non-reacting mixtures of fuel simulants for mixing experiments is not new and has been extensively utilized as a screening technique for scramjet fuel injectors. In this study, Reynolds-averaged simulations are utilized (RAS) to systematically verify the implicit assumptions used by the EIMP. This is accomplished by first performing RAS of mixing for two injector configurations at planned nominal experimental conditions. The mixing parameters of interest, such as mixing efficiency and total pressure recovery, are then computed and compared to the values obtained from RAS under the true enthalpy conditions and using helium and hydrogen. Finally, the impact of combustion on mixing, often deemed small enough to neglect at hypervelocity conditions, is assessed by comparing the results obtained from the hydrogen-fueled reacting and non-reacting RAS. For reacting flows, in addition to mixing efficiency and total pressure recovery, the combustion efficiency and thrust potential are also considered. In all of the simulations, the incoming air Mach number and the fuel-to-air ratio are the same, while the total pressure, total enthalpy, and the fuel simulant vary depending on the case considered. It is found that under some conditions the "cold" flow experiments are a good approximation of the flight.
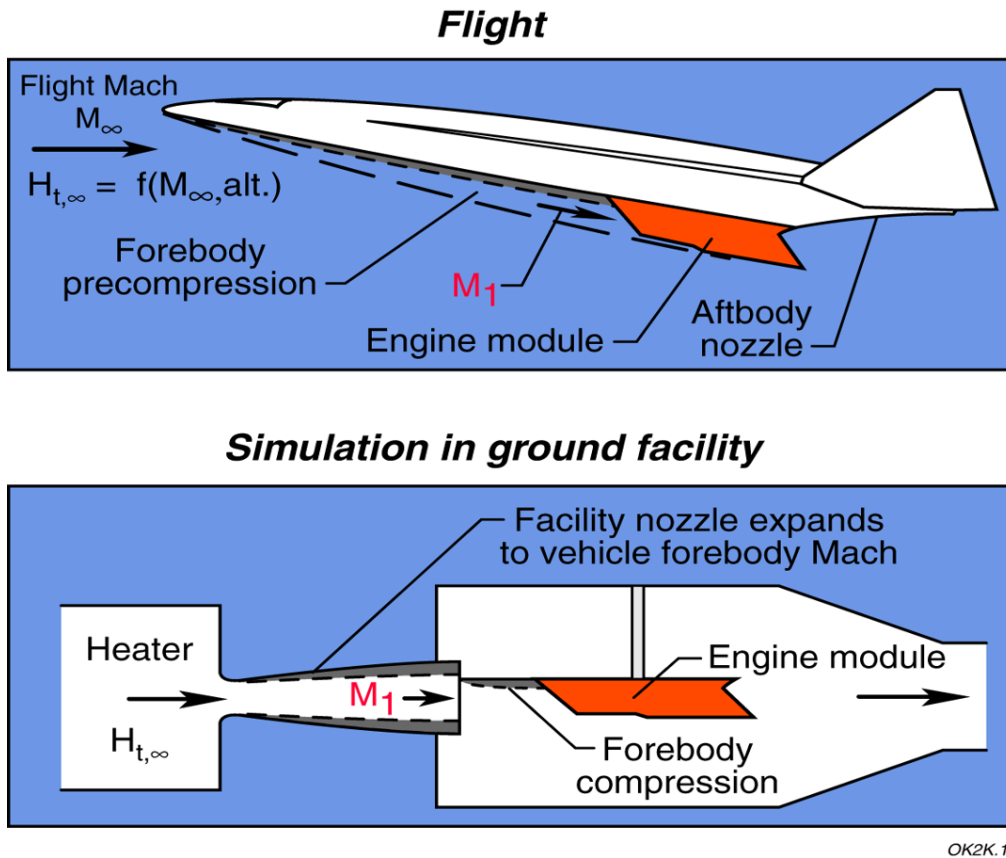
Figure 1: Conceptual illustration depicting a common approach to ground experimentation for high-speed propulsive flows.

INTRODUCTION

Ground experimentation for high-speed propulsive flows often involves compromises that result in the departures from the desired test conditions. These departures can be either driven by financial requirements, for example prohibitive costs associated with construction of new labs and facilities or budgetary pressures associated with building expensive experimental hardware, or technical limitations associated with the size and operational capabilities (e.g., total pressure, total enthalpy, or facility air vitiation effects) of the existing facilities. Figure 1 graphically summarizes the typical approach to ground experimentation for high-speed propulsion. In this figure, the high-speed vehicle, traveling at supersonic speeds, causes a bow shock to develop due to the forebody. This bow shock precompresses the flow, which then enters the vehicle engine module. Additionally, the precompressed forebody flow develops a boundary layer, which induces drag onto the vehicle and heats the vehicle forebody surface. To reproduce the flow entering the engine module on the ground, the aerothermal properties of the precompressed flow, including the boundary layer properties, and any heat loss to the forebody, should be matched. This could be achieved by heating a flow on the ground to a value of the total enthalpy computed at a desired flight point and expanding this flow through a facility nozzle to the desired value of the post-compression Mach number, denoted as M_1 in Fig. 1. The heating requirements are proportional to the value of the flight Mach number, M_∞. Depending on the flight point considered, these requirements could be severe; and for hypervelocity flows, where over 95% of energy is associated with the kinetic energy of the flow, could require temperatures in excess of those that could dissociate the air, thereby causing vitiation of the air. If heating is produced by combustion, then the air could be vitiated by combustion products such as water vapor and/or carbon dioxide. Furthermore, rapidly

2

expanding the chemically-equilibrated heated air containing rotationally and vibrationally excited species through a facility nozzle could further thermodynamically "vitiate" the mixture by "freezing" the mixture of gases in their exited states.[1,2] The mass flow rate and the density of the expanded flow that a ground simulation can support is proportional to the total pressure that can be achieved in the air heater. If for any reason the ground simulation cannot reproduce the flight conditions, then the existing gap between ground and flight must be at least understood, if not quantified, for the experiments to be useful.

After the air flow enters the engine module, fuel must be injected, mixed, and burned to energize the flow, and then expanded through the aft nozzle to produce thrust. However, designing devices capable of robust hypersonic air-breathing operation, characterized by rapid fuel-and-air mixing and short combustion times while ensuring flame stability over a wide range of speeds, has proven difficult. Attempts at improving fuel injection to enhance fuel-and-air mixing, while simultaneously reducing total pressure losses, have received a great deal of attention over the years. While some total pressure loss is thermodynamically unavoidable and occurs as a direct result of the desired effect of molecular mixing, any losses beyond this amount reduce the thrust of the engine.

Some of the mixing enhancements considered include: variable-angle injection, non-circular injectors, and small and large vortex/swirl generating tabs and ramps. For high Mach number internal flows, where combustor residence times are increasingly small, and compressibility effects may further suppress mixing,[3–8] poor injector performance leads to unnecessarily long combustor lengths, and therefore, increased drag and reduced thermal performance of the engine. In an effort to achieve more rapid mixing at high speeds, designers have typically considered multiport fuel placement devices, such as slender, often swept, struts protruding into the core flow, and/or large vortex generators, such as swept or unswept ramps that induce large axially-rotating vortices. A good overview was recently provided by Lee et al.[9] While the ramps rely on large vortices to entrain the air and fuel into one another, and enlarge and stretch the fuel-air interface, thereby increasing the fuel-air mixing layer interface area, the struts typically generate few vortices and rely on fuel port features (such as fuel port shape and/or tabs) to enhance small-scale mixing within the developing fuel-air mixing layer. Several ramps or struts are typically used to "fill" the combustor cross section in a manner that provides enough fuel to satisfy the equivalence ratio requirements. An additional benefit, increasingly important in higher Mach number flows, of strut and ramp injection is that the fuel is often injected parallel to the main air flow. In such a configuration, the thrust produced by the aft-facing fuel injector ports augments the thrust generated by the combustion processes. It should be noted that despite the small amount of fuel mass entering the engine, the thrust augmentation from aft-facing fuel injector ports may be significant especially when the fuel is used for cooling of the various vehicle components. In those situations, the aft-facing fuel ports become energy recovery devices by converting heat absorbed in cooling the vehicle components into thrust.

This work focuses on utilizing computational fluid dynamics (CFD) to assess the mixing effectiveness of two classes of injectors, namely a strut, and a ramp under various flow conditions that might be considered experimentally. These conditions range from a low-enthalpy, low total pressure, non-reacting flow to a true flight total enthalpy and total pressure, reacting flow. The low-enthalpy flow conditions correspond to baselines proposed for the Enhanced Injection and Mixing Project (EIMP)[10] being conducted at the NASA Langley Research Center. The EIMP aims to investigate scramjet fuel injection and mixing physics, improve the understanding of underlying physical processes, and develop enhancement strategies and functional relationships between mixing performance and losses relevant to flight Mach numbers greater than 8. The experiments will consider a "direct-connect," subcomponent-level approach and utilize a Mach 6 nozzle to simulate the combustor entrance flow of a scramjet engine. However, while the value of the internal flow Mach number matches that expected in flight, the value of the total enthalpy for these experiments is limited by the thermal-structural limits of the uncooled hardware. For the EIMP experiments, this correspond to about Mach 4.25 flight enthalpy at a flight dynamic pressure of 1500 psf. Furthermore, the fuel simulant is helium, not hydrogen. The use of low enthalpy, "cold," flows and non-reacting mixtures of fuel simulants for mixing experiments is not new[11,12] and has been extensively utilized as a screening technique for scramjet fuel injectors. The present work will address the extent to which low enthalpy, non-reacting, experiments can reproduce mixing characteristics of injectors in hypervelocity flight.
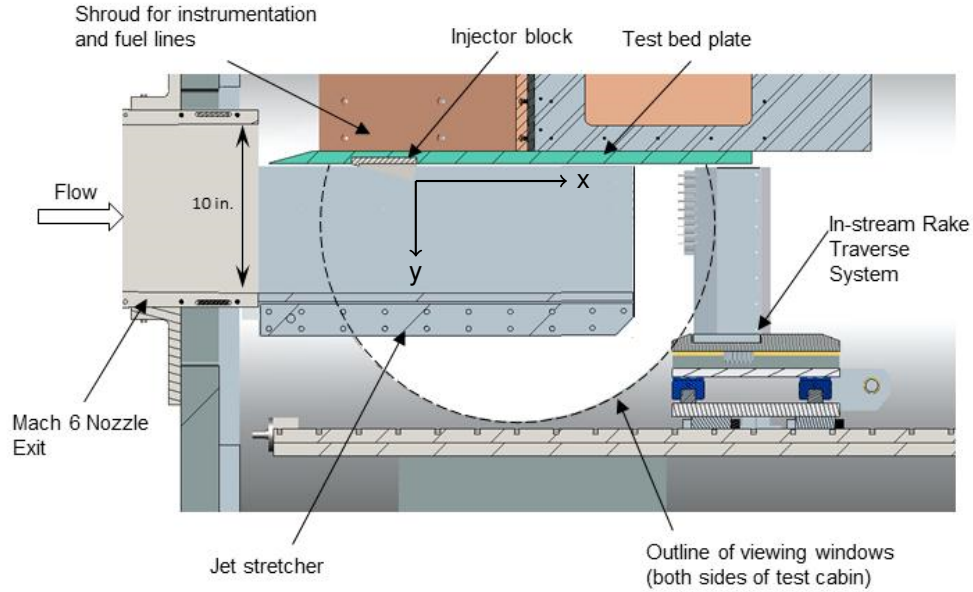
Figure 2: Cross section of the experimental cabin with the facility nozzle, test bed plate, jet-stretchers, instrumentation shroud, and the in-stream rake probe indicated. The figure shows the configuration as installed in the wind tunnel, however, all CFD simulations were performed with the positive y-direction in the plate-normal direction, which is pointing toward the ground.

The paper is organized as follows: first, a short overview of the EIM project, and a description of the experimental conditions are provided. Next, a general description of the strut and ramp injector geometries, and flow features are provided. The metrics of mixing considered here are discussed next. The discussion of numerical considerations that apply to all simulations is presented also. The results and discussion illustrate the impact of various experimental conditions on mixing and losses. The paper is then summarized and several ongoing and future efforts are described.

INJECTOR GEOMETRIES AND SIMULATED FLOW CONDITIONS

Two types of injectors are used in the current simulations. Both have been previously studied by Baurle et al.[13] under "cold" flow conditions at the combustor entrance Mach number of 4.5. However, unlike the simulations of Baurle et al.,[13] which configured the injectors in a closed duct and interdigitated fashion, the current simulations include an infinite row of injectors on an open flat plate. The open flat plate is considered to numerically represent the experimental configuration of the Enhanced Injection and Mixing Project (EIMP) at the NASA Langley Arc-Heated Scramjet Test Facility (AHSTF). While no experimental data is yet available, EIMP experiments entail testing various fuel injection devices mounted on an open flat plate located downstream of a Mach 6 facility nozzle, which simulates the combustor entrance of a flight vehicle traveling at a Mach number of about 14 to 16. Figure 2 shows the cross section of the experimental apparatus mounted in the 4 ft. diameter test cabin. Noted on the figure are the flat plate test bed platform with its leading edge positioned several inches below the top wall of the Mach 6 facility nozzle. The flow is from left to right. The flat plate is 28.87 inches long tip-to-tail and 32 inches wide. The injector block section provides an interchangeable interface to which various injector designs can be mounted. A row of several injectors can be mounted with the fuel injection plane located at 8.87 inches downstream from the leading edge of the plate. The facility air flows over the injector bodies and mixes with the fuel simulant downstream of the injection plane. Also noted in Fig. 2 are the in-stream rake traverse system (used for
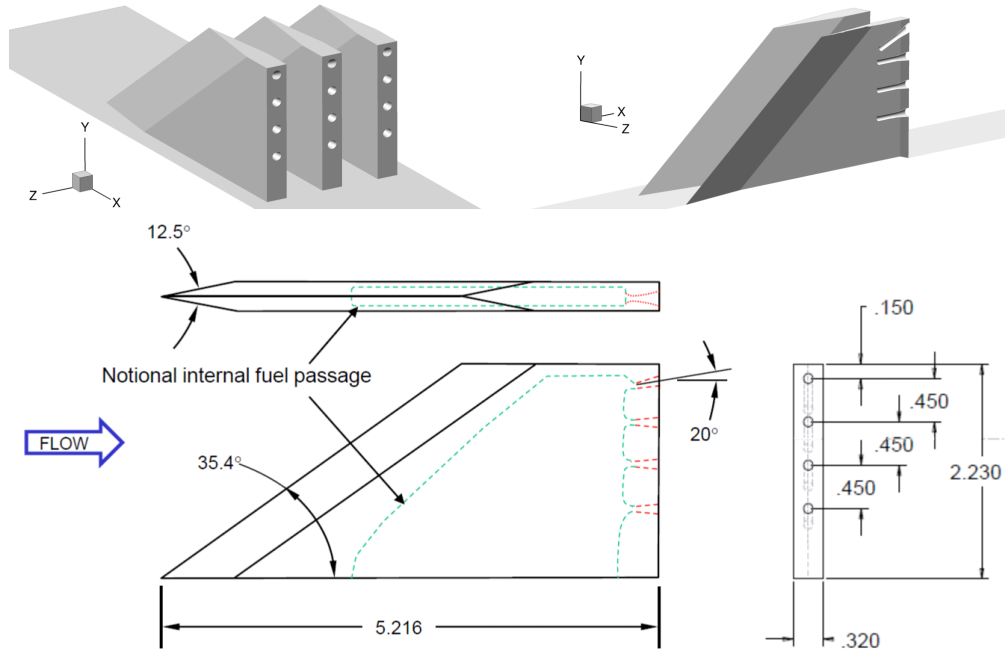
Figure 3: Isometric views and dimensional details of the baseline strut injector. Linear dimensions are in inches.

pitot pressure, total temperature, and gas sampling), the jet stretchers, and the instrumentation shroud located on the back side of the flat plate. The figure shows the orientation of the experimental apparatus as is installed in the wind tunnel facility. In all subsequent CFD simulations the positive y-direction is oriented in the plate-normal direction, which in this figure is pointing toward the ground. Further details about the experimental setup and EIMP are presented in Cabell et al.[10] The experiment is intended to provide a test-bed flexible enough for rapidly testing a variety of different fuel injector devices and injection strategies. Current experiments focus on studying fuel injection and mixing processes in the absence of heat release by utilizing helium as a fuel simulant. Furthermore, these experiments are referred to as "cold" because the total temperatures of the facility air are bounded between the condensation limit for the expanded facility air and the thermal-structural limits of the uncooled hardware. The former and latter correspond to 727.8, and 977.8 K, respectively, and are both significantly lower than the relevant flight total temperature. Only the upper limit of the total temperature is considered for the current simulation of the EIMP case because previous work[1] has shown that the results obtained for the lower limit are similar.

The first injector is a slender swept strut protruding into the flow. Strut injectors have several advantages in hypervelocity flow applications. First, they can be designed to place the fuel where it is needed, thereby alleviating the need to consider fuel penetration issues and focusing only on the injector spacing. Second, the injector ports on a strut are typically aligned parallel to the flow, which allows for the injected fuel streams to augment the thrust of the engine. The potential downsides of a strut injector are the structural integrity and cooling requirements needed for its slender body, drag that it induces on the flow by the obstruction it generates, and the oblique shocks that emanate off its leading edge. The shock waves introduce total pressure losses, pass through and interact with one-another, and reflect off the sidewalls of the combustor. The interactions of shock waves with the sidewall boundary layers has the potential to separate the flow and introduce local hot spots, as well as, additional flow blockage. However, these shock waves also introduce mixing enhancement via the effect of the baroclinic torque as they pass through the variable density interfaces of fuel-and-air mixing plumes and introduce localized vorticity. Views of the strut, and its dimensional details are shown in Fig. 3. The x, y, and z denote the streamwise or downstream, vertical or wall normal, and cross-stream dimensions, respectively. In the current simulations, the struts are placed
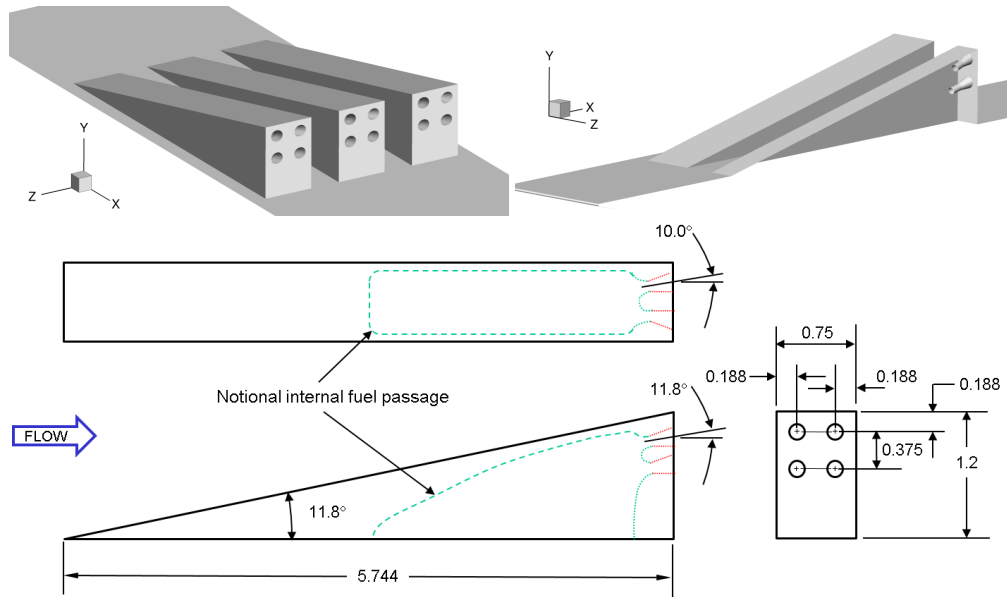
Figure 4: Isometric views and dimensional details of the baseline ramp injector. Dimensions are in inches.

0.9 inches apart. This spacing is the same as that found between the interdigitated strut injectors of Baurle et al.[13] Each strut injector has four fuel injector ports. This is different from the interdigitated struts of Baurle et al.,[13] which only have three injector ports. The second injector port from the bottom is not needed in the interdigitated configuration because the staggered injector port of the adjacent strut is relied upon to fill this portion of the cross sectional area with fuel. Each injector port has a throat diameter of 0.083 inches followed by a conical expansion area with a half-angle of 6 degrees that is designed to expand hydrogen to an exit Mach number of about 2.6.

The second injector is an unswept ramp. Unlike the strut, the ramp injector does not protrude as much into the flow but is wider and therefore, can introduce as much or more blockage. The ramp injector generates a counter-rotating vortex pair (CVP) on each side of the ramp as the flow passes over the ramp and through the gaps between the ramps, which convects the injected fuel upwards, towards the core of the flow, and fills the intended fueling area. In addition to inducing the upward entrainment, the CVP stretches the fuel-air interface thereby increasing the surface area over which the molecular viscosity can act to mix the fuel and air. Because the strength of the CVP depends on both the geometry of the ramp, and the incoming air flow conditions, designing a ramp injector that robustly fills its intended fueling area across a range of flight conditions is more challenging than a strut. Similarly to the strut, the ports of the ramp injector are also mostly aligned parallel to the flow and allow for injected fuel streams to augment the thrust of the engine. However, the ports are angled slightly up and to the side to aid in directing the fuel streams toward the CVP. The ramp injectors also generate an oblique shock due to its inclined surface. Similarly to the shock waves generated by the strut injector leading edge, the ramp shock induces total pressure losses, and reflects off the top and/or bottom surfaces of the combustor where it interacts with the boundary layer and can separate it inducing further losses, increased heat transfer to the wall, and flow blockage. Because the ramp induces only a single oblique shock, the total pressure losses are expected to be smaller than those of the struts, but the potential for mixing enhancement via the baroclinic torque is also reduced. Views of the ramp, and its dimensional details are shown in Fig. 4. In the current simulations, the adjacent ramps are placed 1.2 inches apart. This spacing is also the same as that found between the interdigitated ramp configuration of Baurle et al.[13] Each injector port has a throat diameter of 0.108 inches followed by a conical expansion area with a half-angle of 10 degrees that is designed to expand hydrogen to an exit Mach number of about 2.6.

Table 1: Qualitative description of the simulation cases in the current study.

	Case Abbrv.	Mach No.[†]	P_0[‡]	T_0[‡]	Wall BCs @ T (K)	Air	Fuel @ T_0 (K)	React.
1	PoG/ToG/He	6	P_0^G	T_0^G	Adiabatic	1% NO[§]	He @ 300	N
2	PoG/ToF/He	6	P_0^G	T_0^F	1D HT @ 1200	1% NO[§]	He @ 300	N
3	PoF/ToF/He	6	P_0^F	T_0^F	1D HT @ 1200	Clean[¶]	He @ 1200	N
4	PoF/ToF/H2	6	P_0^F	T_0^F	1D HT @ 1200	Clean[¶]	H2 @ 1200	N
5	PoF/ToF/H2/R	6	P_0^F	T_0^F	1D HT @ 1200	Clean[¶]	H2 @ 1200	Y

[†] Nominal value at combustor entrance.

[‡] superscripts F and G denote air conditions at the combustor entrance in flight and ground simulations, respectively

[§] 21% O_2, 78% N_2, 1% NO

[¶] 21% O_2, 79% N_2

It should be noted that because the current simulations are for an open plate configuration, they do not take into account the area expansion that is typically used to relieve the area blockage introduced into a ducted flowpath by struts or ramps. In addition to counteracting the area blockage, this area relief causes the flow to expand through the gaps between the injectors and further enhance the strength of the CVP for the ramp configurations. Furthermore, the area expansion naturally ends at the base of the injector where the combustor walls typically turn parallel again (or continue at a very shallow angle of up to few degrees). This turning of the flow induces a shock wave at the base of the injector, which introduces additional total pressure losses but also enhances the fuel-and-air mixing via baroclinic torque effects, as discussed above. The effects associated with the area expansion are not captured in the current simulations. Finally, because the goal of the current study is to assess the impact of testing fuel injectors designed for hypervelocity flight in "cold" ground simulations, the geometry of the injectors and their fuel ports is fixed for all conditions.

Five different flow conditions that could be reasonably thought of as appropriate for the experiments are considered. These cases are qualitatively described in Table 1. In this table, and throughout the rest of this paper, all of the cases are abbreviated using combinations of mnemonics, namely PoG, ToG, PoF, and ToF, that denote the combustor air inflow total properties for the ground and flight total pressure and total temperature, respectively. For example, the second entry in Table 1, abbreviated as PoG/ToF/He, describes the combustor air inflow properties corresponding to the ground facility total pressure and flight total temperature with helium as a fuel simulant.

The first case, abbreviated as PoG/ToG/He, corresponds to the nominal baseline conditions used in the ground experiments to be conducted as a part of the EIMP. Because an electrical arc is used as a heat source for the facility air, a portion of the air is heated well beyond what is needed for the experiments. The temperatures are usually high enough to cause dissociation of air and produce measurable quantities of minor air species, such as NO.[14] Downstream of the arc-heater, additional air is added to reduce the value of the total enthalpy to that desired. The mixture is allowed to equilibrate to the target total temperature inside the plenum. Nevertheless, NO remains as a vitiate. In the EIMP experiments, this trace amount of NO enables nonintrusive flow visualization[15] via NO planar laser induced fluorescence (NO-PLIF). The current simulations assume that about 1% NO exists in the facility air stream and replaces 1% N_2. Such a small amount of vitiate is not expected to have a strong impact on the non-reacting mixing study as compared to clean air. Because the experimental hardware was designed to operate for long durations uncooled, the simulations were conducted with adiabatic wall boundary conditions for the flat plate. However, since room temperature helium is flowing through the internal passages of the strut and ramp injectors, a modified isothermal boundary condition, modeling one-dimensional (1D) heat transfer through a thin wall, is used for the strut and ramp bodies. The internal wall temperature is set to the value of the total temperature of helium, which was 293.15 K. The facility total pressure is 4.309 MPa. This value corresponds to a structural limit of the facility and includes a margin of safety.

Table 2: Flight free stream conditions in the current simulations.

Alt. (km)	Mach No.	Q (kPa)	P (kPa)	T (K)	T_0[†] (K)	P_0[†] (MPa)
36.6	14.94	71.82	0.4603	249.2	8748.4	1294.7

[†]Value based on frozen composition of air

The second case, denoted by PoG/ToF/He, corresponds to the same ground experiment in the same facility as above, except the stagnation enthalpy has been increased to match a hypervelocity flight total enthalpy. The flight total enthalpy is obtained by proposing a hypothetical inlet process that compresses the free stream air to half an atmosphere and a Mach number of about 6 at the combustor inflow. The inlet is further assumed to have a 95% isentropic efficiency and 99% adiabatic efficiency.[16] Further assuming a nominal vehicle flight path along a constant dynamic pressure trajectory of 1500 psf, and using the standard atmosphere tables,[17] gives a nominal flight condition, which in this case corresponds to about Mach 15 flight at an altitude of about 120 kft. The kinetic energy efficiency of this inlet is about 98%. The exact free stream conditions obtained by following the above outlined approach and used in the current simulations are shown in Table 2. It should be noted, however, that because of the very high value of the flight Mach number, the values of the total temperature and total pressure presented here are used only as indicators of the energetic content of the flow, and for the purpose of computing the desired combustor entrance flow conditions.

Under the high enthalpy conditions, the experimental hardware would have to be cooled. A reasonable operating temperature corresponds to 1172.6 K, which is about the maximum service temperature of the Hastelloy X high temperature alloy, as reported by Haynes International. This alloy material could have been used for the construction of the flat plate. For the simulations of this case, the modified 1D isothermal boundary condition is used for both the flat plate, and the injector bodies, assuming they are constructed of Hastelloy X and operate with internal wall temperatures set to 1172.6 and 293.15 K, respectively. As with the previous case, the helium is at the room temperature.

The third case, denoted by PoF/ToF/He, corresponds to a ground experiment where both the total enthalpy and total pressure match those at the entrance to the combustor in flight and no vitiates are present in the facility air. Helium is still used as a fuel simulant to investigate mixing in isolation from reaction. However, to better represent a scenario in flight where the fuel would likely be used as a cooling medium, helium is now heated to the temperature of 1172.6 K. Therefore, for the simulations of this case, when the modified 1D isothermal boundary condition is used, the internal wall temperatures for both the flat plate, and the injector bodies, are set to 1172.6 K.

The last two cases, denoted by PoF/ToF/H2 and PoF/ToF/H2/R, are similar to the previous case in that the total enthalpy and total pressure correspond to the values found at the combustor entrance in flight. However, in both cases, helium has been replaced with hydrogen, which is also heated to 1172.6 K. These cases consider mixing-only, and mixing and reacting flow, respectively. For the latter, since of primary interest is the impact of heat release on mixing, the mixed-is-burned (or eddy break-up) combustion model of Magnussen and Hjertager[18] is used. This model is modified to include a limiting reaction rate by further incorporating a global finite-rate mechanism of Marinov et al.[19] Qualitatively, the model allows for combustion and heat release to take place soon after the mixing of fuel and air, but not as rapidly as could be achieved by assuming equilibrium chemistry, which would be unphysical for the current conditions, and further result in combustion efficiency values nearly identical to those of the mixing efficiency. These two cases allow us to consider the two limiting cases that could occur in the engine and correspond to the extinguished conditions and fully burning ones, respectively.

In all of the simulations, the equivalence ratio, defined as the ratio between mass flow rate of fuel and air divided by the stoichiometric value, is kept at one. The stoichiometric value of the mass fuel-to-air ratio is set to that of hydrogen and air for all cases and is equal to 0.0292. The mass flow rate of air is computed using the nominal facility air flow properties and the "intended" fueling area for each injector.

Since current injectors are identical to those previously investigated in a ducted configuration by Baurle et al.[13] the intended fueling areas can be obtained by examining those configurations. For the strut injector, the intended fueling area is equal to the strut spacing (0.9 inches) times the height of the isolator duct found in Baurle et al.[13] (2.25 inches). For the ramp injector, however, the injector spacing (1.2 inches) is multiplied by the half-height of the isolator duct. Since the current ramp configuration is neither interdigitated nor contains area relief, the penetration is expected to be suppressed, and therefore, more inline with a half-height of the isolator duct. This modification to the intended fueling area is not needed for fuel placement devices such as the strut. The total mass flow rate of fuel is obtained by multiplying the mass-flux rate of air by the intended fueling area and the stoichiometric value of the fuel-to-air ratio.

The details of all of the flow parameters used in the current simulations are shown in Table 3. Both the properties of air and fuel are presented. The subscripts f and a denote fuel and air flow streams, respectively. In addition to the quantities needed for the simulations, a few nondimensional quantities are also shown. These are, the unit Reynolds numbers per inch for the air and fuel streams, velocity difference parameter, $\Delta \mathrm{U}$, the convective Mach number, $\mathrm{M_c}$, and the ratios of the density, $\rho_\mathrm{f} / \rho_\mathrm{a}$, static pressure, $\mathrm{p_f} / \mathrm{p_a}$, and dynamic pressure, J between the fuel and air stream. These values are computed based on the combustor entrance flow conditions for the air and the expanded flow conditions at the exit of the injector ports for the fuel. These nondimensional quantities have been found to be relevant to the injection and mixing processes in canonical problems.[3,20,21]

METRICS OF INTEREST

A number of different metrics for thrust performance, mixing and combustion efficiency, and associated thermodynamic losses exist with the most detailed analysis proposed by Riggins et al.[22] For the current study the following were chosen: the integrated (in the cross-stream and vertical directions) forms of the total pressure recovery, mixing efficiency based on stoichiometric proportions of fuel and air, thrust potential, and combustion efficiency based on fuel depletion. The total mass-flux-weighted pressure recovery is defined as:

$$P_t^{rec} = \frac{\int P_t \rho U dA}{\int P_{t_\infty} \rho U dA} \tag{1}$$

where P_t is the total pressure, ρ is the density, U and dA are the velocity magnitude and the incremental area projected in the streamwise direction, respectively. This parameter is proportional to the difference between sensible entropies computed at the total and static values of the temperature, and therefore, gives a measure of the thermodynamic losses. For purely mixing simulations, the total pressure recovery quantifies the losses due to the drag on the injector bodies and the surface of the flat plate, the mechanical stirring induced by injector bodies (especially the ramp), the turbulence, and the molecular mixing. For reacting simulations, the total pressure recovery is further reduced by the chemical reactions, therefore, the values of the total pressure recovery obtained from the purely mixing simulations could be thought of as the maximum achievable for a given injector. Because chemical reactions reduce the total pressure recovery, which can be interpreted as a loss, yet energize the flow via heat release, which can be expanded into thrust, there is a need for another metric, which can more objectively quantify the potential performance of the flowpath. The most direct metric that can achieve this is the thrust potential. This metric is obtained by expanding one-dimensional values of the flow variables at each streamwise location through an ideal, isentropic and adiabatic, thrust nozzle. In the current work, this thermodynamic process is evaluated until the flow reaches its free stream value of the static pressure. The thrust potential is then computed from:

$$TP(N) = \dot{m}u_{exit} + (p_{exit} - p_\infty)A_{exit} \tag{2}$$

where TP is the thrust potential, and $\dot{m}$, u_{exit}, p_{exit}, A_{exit}, and p_∞ are the mass flow rate, velocity, pressure, and the area at the thrust nozzle exit plane, and the free stream static pressure, respectively. Since the flow expands to free stream static pressure, the second term in the above equation is identically zero. This metric represents an ideal potential thrust that could be obtained when a flowpath of interest is truncated

Table 3: Global parameters of interest for the strut and ramp injector configurations. The last set of rows for both strut or ramp configuration contains a few ratios of interest between the fuel and air streams, where the subscripts f and a denote fuel and air streams, respectively. Quantities that are common among different cases are highlighted in bold font.

	Property	PoG/ToG/He	PoG/ToF/He	PoF/ToF/He	PoF/ToF/H2
Air	Mach	**6.356**	**6.356**	**6.356**	**6.356**
	P0 (MPa)	**4.309**	**4.309**	295.4	295.4
	T0 (K)	977.8	8654.5†	**8672.8**	**8672.8**
	P (kPa)	1.808	0.739	**50.66**	**50.66**
	T (K)	112.4	1295.0	**1297.8**	**1297.8**
	u_a (m/s)	1352.6	4454.9	**4461.1**	**4461.1**
	Re/in x10e6	315.0	6.86	**469.2**	**469.2**
	$FAR\|_{st}$	**0.0292**	**0.0292**	**0.0292**	**0.0292**
Strut	Area‡		0.9in x 2.25in		
	$\dot{m}_a$ (kg/s) x10e-3	98.76	11.53	**789.5**	**789.5**
	Mach	**2.977**	**2.977**	**2.977**	2.608
	P0 (MPa)	0.224	0.0261	3.58	5.384
	T0 (K)	**293.15**	**293.15**	**1172.6**	**1172.6**
	P (kPa)	7.205	0.8416	115.2	263.9
	T (K)	**74.14**	**74/14**	296.6	504.5
	$\dot{m}_f$ (kg/s) x10e-3	2.884	0.337	**23.05**	**23.05**
	u_f (m/s)	**1508.2**	**1508.2**	3016.4	4447.0
	Re/in x10e6	352.6	41.18	1129.6	1757.0
	$\Delta U^\S$	0.0544	-0.4941	-0.1932	-0.0017
	$M_c^\P$	0.2163	2.4402	0.8423	0.0059
	ρ_f / ρ_a	0.8371	2.7571	1.3805	0.9364
	p_f / p_a	3.9845	1.1386	2.2739	5.2098
	$J^\|$	1.0408	0.3160	0.6311	0.9364
Ramp	Area‡		1.2in x 2.25in / 2		
	$\dot{m}_a$ (kg/s) x10e-3	65.84	7.690	**526.3**	**526.3**
	Mach	**2.956**	**2.956**	**2.956**	2.594
	P0 (MPa)	0.0882	0.0103	1.410	2.120
	T0 (K)	**293.15**	**293.15**	**1172.6**	**1172.6**
	P (kPa)	2.9114	0.3401	0.0466	0.1063
	T (K)	**74.91**	**74.91**	299.6	507.7
	$\dot{m}_f$ (kg/s) x10e-3	1.922	0.2245	**15.37**	**15.37**
	u_f (m/s)	**1505.6**	**1505.6**	3011.1	4436.4
	Re/in x10e6	139.8	16.33	447.97	698.5
	$\Delta U^\S$	0.0535	-0.4948	-0.1941	-0.0028
	$M_c^\P$	0.2119	2.4371	0.8428	0.01026
	ρ_f / ρ_a	0.3348	1.1026	0.5521	0.3747
	p_f / p_a	1.6100	0.4601	0.9188	2.0982
	$J^\|$	0.4149	0.1259	0.2515	0.3747

† Value based on the frozen composition of air. Total enthalpy is constant for all combustor entrance flight conditions. The small difference in T_0^F from other cases is due to air vitiation with 1% NO.

‡ Intended fueling area for the injector

§ Velocity difference parameter, $(u_f - u_a)/(u_f + u_a)$

¶ Convective Mach number, $|u_f - u_a|/(c_f + c_a)$, c denotes the speed of sound.

$^\|$ Dynamic pressure ratio, $(\rho_f u_f^2)/(\rho_a u_a^2)$.

at a given streamwise location and coupled at that location to an ideal thrust nozzle. All of the losses in the value of the total pressure previously discussed for the purely mixing case would still appear as a decrement to the value of the thrust potential, however, the chemical reactions, which energize the flow, could increase the value of the thrust potential.

The mixing efficiency is defined in this work following Mao et al.:[12]

$$\eta_m = \frac{\int \alpha_R \rho U dA}{\int \alpha \rho U dA} \tag{3}$$

where the integration is over a single streamwise, x-plane of interest, and α is the fuel or oxidizer mass fraction depending on whether the global equivalence ratio is less than or greater than 1, respectively. Quantity α_R is defined as the amount of fuel or oxidizer that would react if complete reaction took place without further mixing, i.e.,

$$\alpha_R = \begin{cases} \alpha, & \alpha \leq \alpha_{st} \\ \frac{\alpha_{st}}{1-\alpha_{st}}(1-\alpha), & \alpha > \alpha_{st} \end{cases} \tag{4}$$

where α_{st} is the stoichiometric value of fuel or oxidizer mass fraction. For cases with overall equivalence ratio of one, either fuel or oxidizer can be used in place of α. But choosing fuel has a minor benefit of clarifying somewhat the meaning of Eq. (4), which becomes:

$$\alpha_R = \begin{cases} Y_f, & Y_f \leq Y_{f,st} \\ FAR_{st} \, Y_a, & Y_f > Y_{f,st} \end{cases} \tag{5}$$

where Y denotes mass fraction, and subscripts f and a denote fuel and air streams, respectively. It is clear from the above equation that if the local value of the mass fraction of fuel is less than its stoichiometric value then that amount is "counted" as fully mixed because there is sufficient amount of air to completely deplete the fuel if reactions were allowed. However, when the local value of the fuel mass fraction is greater than its stoichiometric value then the only part that could react is that which is in stoichiometric proportion to the local value of the mass fraction of the air. Therefore, only that portion is counted as being mixed in Eq. (3). The stoichiometric value of the hydrogen mass fraction is 0.0285. The mixing efficiency formula of Mao et al.[12] can also be used to analyze mixing in the reacting simulations, however, since fuel and oxidizer are consumed to make combustion products, care must be taken to consider either the elemental mass fractions of fuel or oxidizer (i.e., mass fractions of all elements that originate in either fuel or oxidizer streams), or (if available) the inert species.

The combustion efficiency quantifies how completely a given flowpath is able to process a mixture of fuel and air into combustion products, thereby enabling heat release into the flow. There exists a number of combustion efficiency definitions that include combinations of the total temperature, the enthalpy or enthalpy of formation as a function of local equilibrium composition, fuel/oxidizer depletion or combustion product production. In this work, the simplest definition based on the fuel mass fraction depletion is considered, i.e.,

$$\eta_c = 1 - \frac{\dot{m}_f}{\dot{m}_{f,tot}} \tag{6}$$

where the $\dot{m}_f$ and $\dot{m}_{f,tot}$ are the integrated mass flow rate of fuel at a streamwise location of interest, and the total fuel flow rate, respectively. For mixing-only simulations, the above quantity is identically zero, whereas for reacting simulations its value increases monotonically to one when all of the fuel has been depleted. For fuel-rich simulations, the formulation based on the oxidizer mass fraction depletion would be appropriate.

NUMERICAL CONSIDERATIONS

The numerical simulations were performed using the Viscous Upwind aLgorithm for Complex flow ANalysis (VULCAN-CFD) code.[23] VULCAN-CFD is a multi-block; structured-grid, cell-centered, finite-volume solver

Table 4: Grid densities used in the current simulations.

	Strut	Ramp
Coarse	4,921,682	4,057,382
Medium	39,373,456	32,459,056
Fine	314,987,648	259,672,448

widely used for all-speed flow simulations. For this work, Reynolds-averaged simulations (RAS) were performed. The advective terms were computed using a Monotonic Upstream-Centered Scheme for Conservation Laws (MUSCL) scheme[24] with the Low-Dissipation Flux-Split Scheme (LDFSS) of Edwards.[25] The thermodynamic properties of the mixture components were computed using curve fits of McBride et al.[26] The governing equations were integrated using an implicit diagonalized approximate factorization (DAF) method.[27] The current work used the baseline blended $k-\omega/k-\epsilon$ turbulent physics model of Menter.[28] The Reynolds heat and species mass fluxes were modeled using a gradient diffusion model with turbulent Prandtl and Schmidt numbers of 0.9 and 0.5, respectively. Wilcox wall matching functions[29] were also used, however, their implementation in VULCAN-CFD includes a modification that allows the simulations to recover the integrate-to-the-wall behavior as the value of y+ approaches one. All simulations were converged until the total integrated mass flow rate and the total integrated heat flux on the walls remained constant. This typically occurred when the value of the L_2-norm of the steady-state equation-set residual decreased by about 4-5 orders of magnitude. To conserve the available computational resources, all the simulations were split into an elliptic and a space-marching region. The elliptic region contained the inflow of the domain, the injector bodies, and up to 6.5 inches downstream of the injection plane. The computational cell count was about equal in both regions, but the computational cost associated with solving the space-marching regions was about an order of magnitude lower than that for the elliptic region. A single, fully elliptic simulation on a coarse grid confirmed that this approach indeed did not impact any of the flow features nor the integrated values of the metrics of interest discussed in the previous section.

Three grids, coarse, medium, and fine, each progressively finer by a factor of 2 in each of the three dimensions, were considered. The grid resolutions were the same among the different cases described in Table 3, and for the strut and ramp injectors are summarized in Table 4. The grid density and computational block topology features near the injector bodies for both the strut and ramp injector case are shown for the coarse grid in Figs. 5 and 6. It should be noted that each visible cell in this figure contains 2x2x2 and 4x4x4 cells on the corresponding medium and fine meshes, respectively. In these figures, the injector bodies and fuel ports are colored in blue and red, respectively. For the strut injector cases, a single full strut injector was included in the computational domain. This was done to help alleviate grid skewness issues at the top of the strut, and near the leading edge of the strut. For the ramp injector cases, only half of the ramp injector was included in the computational domain to reduce the grid size requirement. Both grids were generated with GridPro in the vicinity of the injector bodies and the leading edge of the flat plate, and further combined with Pointwise-generated h-blocks to complete the computational definition of the geometry. For both the strut and ramp injectors, the inflow and outflow planes are placed 9 in. upstream, and 25 in. downstream of the fuel injection plane, respectively, which is located at x=0. Since both the inflow and the outflow consist of supersonic flow, static values of the temperature and pressure, and the Mach number are specified at the inflow; and all flow variables are extrapolated at the outflow. The vertical dimension is 6 inches high, which approximates the size of the EIMP facility nozzle core flow.[1] Slip wall boundary conditions are used for the upper boundary of the flow domain. This was done to account for the presence of the jet stretchers used in the EIMP. Since the boundary layer along the jet stretchers is of little interest and is not expected to impact the mixing region, no attempt is made to resolve and model it in the current simulations. Since the simulation domain considers an infinite row of injectors in the cross-stream, the current simulations model the open plate experiment as a large duct. In this model duct, the flow blockage due to injector bodies is 14 and 12.5% for the strut and ramp injectors, respectively. With the exception of the fuel ports, the grid was clustered towards all of the walls with the growth rates varying from 5% to 15%. The values of the distance between the computational cell center and its nearest wall are shown in Fig. 7(a,b). The observed variability is due the specific method employed for near-wall clustering, nevertheless, the corresponding

(a) Grid features on and near the strut injector body
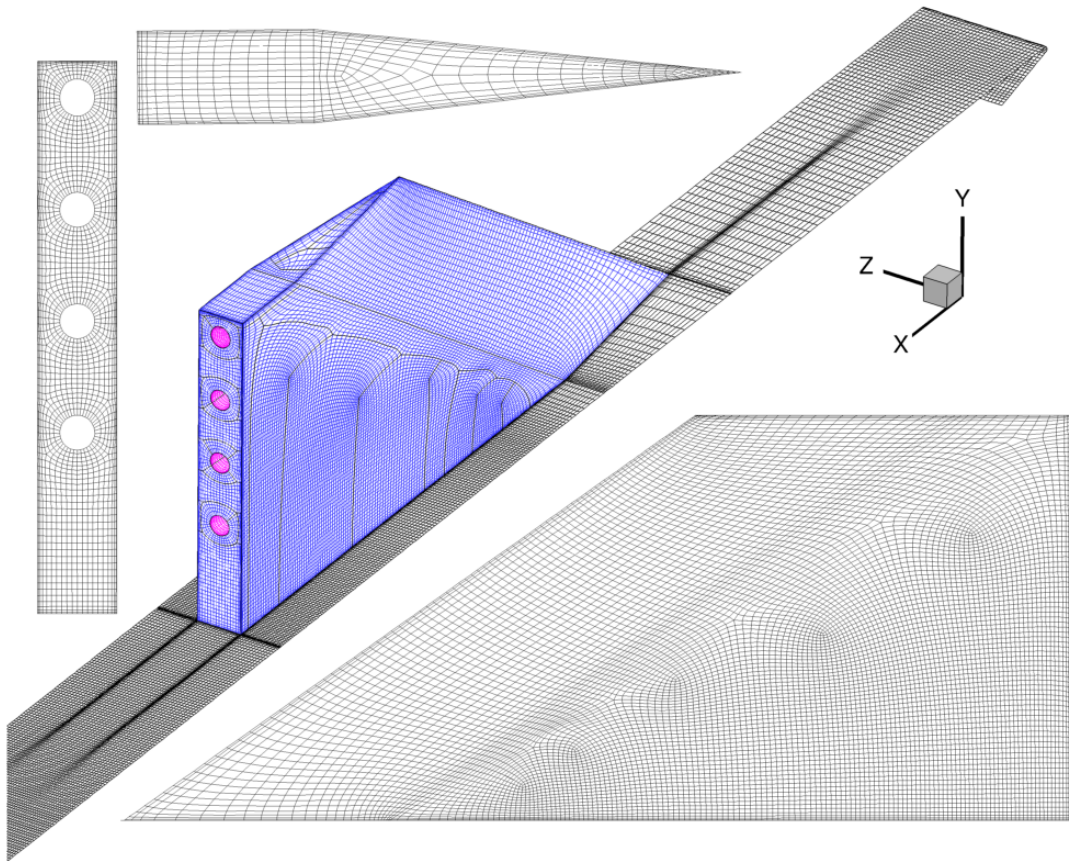
(b) Grid and its block topology along the center-plane near the injector body (Wrapping grid above the injector body is omitted because is does not align with the strut center-plane).
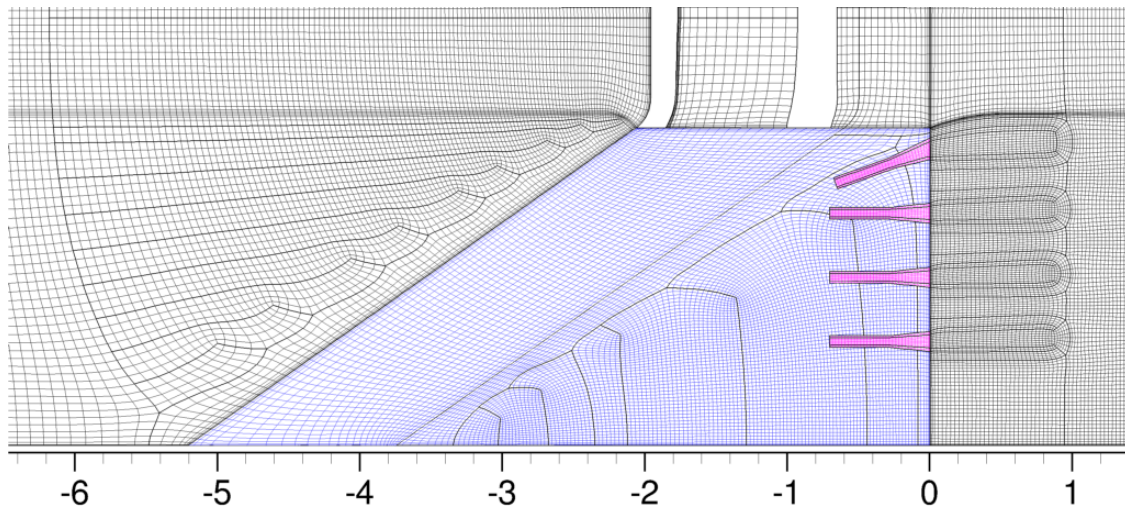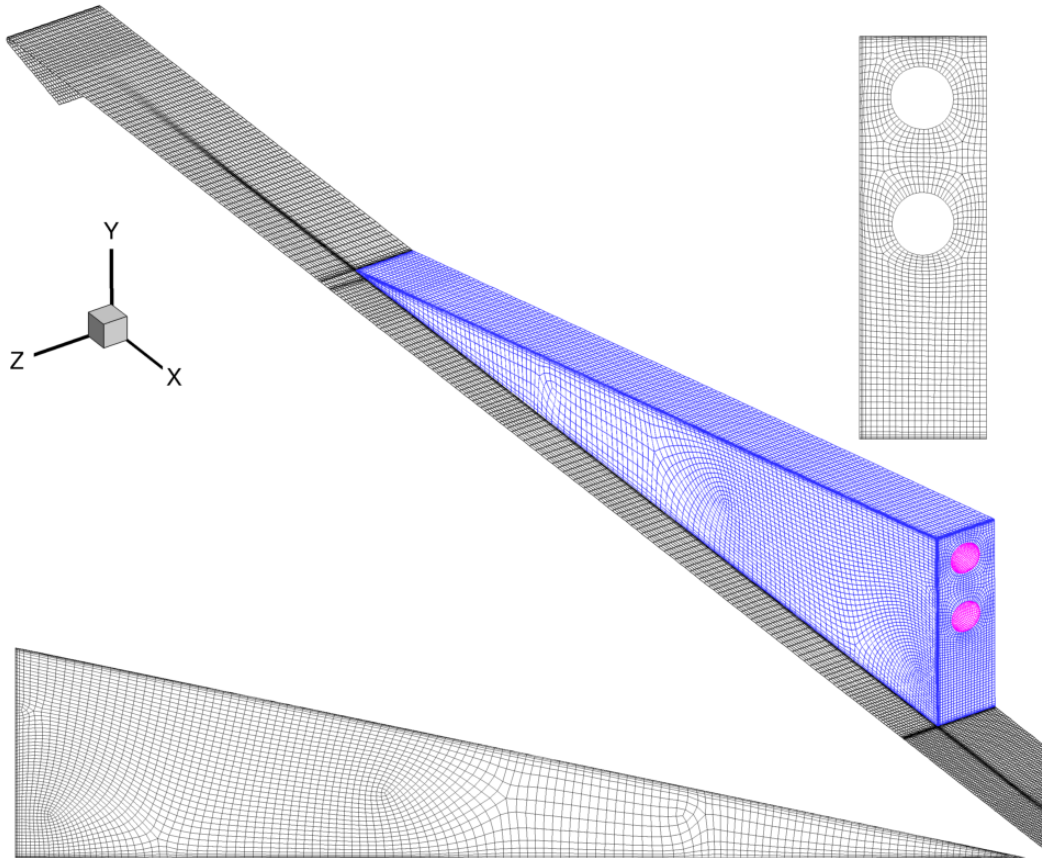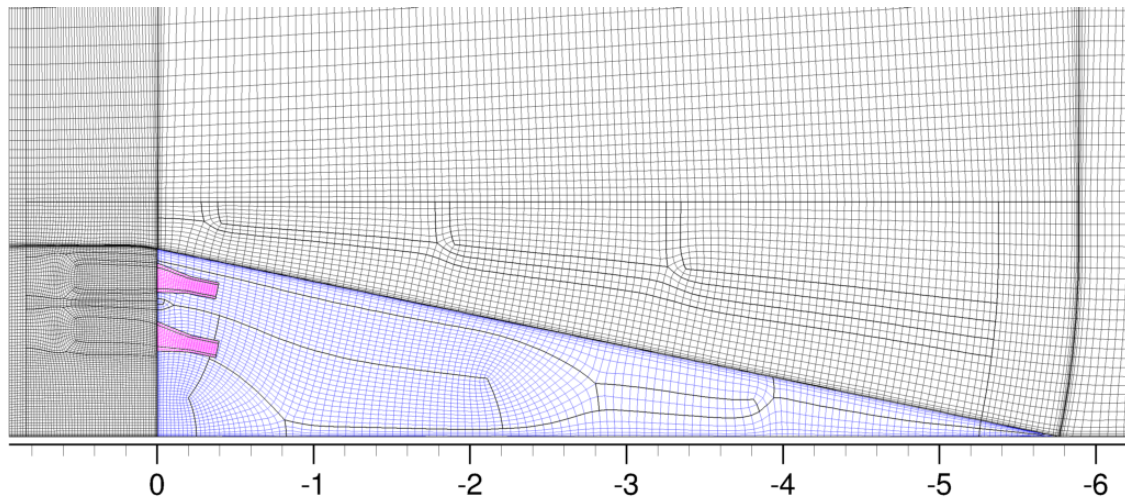

Figure 5: Elements of the coarse grid used for the strut simulations. Each visible cell contains 4x4x4 cells on the corresponding fine mesh. The blue and magenta elements denote the injector body and the fuel ports, respectively.

(a) Grid features on and near the ramp injector body

(b) Grid and its block topology through the center of the injector ports and near the injector body.

Figure 6: Elements of the coarse grid used for the ramp simulations. Each visible cell contains 4x4x4 cells on the corresponding fine mesh. The blue and magenta elements denote the injector body and the fuel ports, respectively.

values of y+ for cases PoG/ToF/He and PoF/ToF/He obtained on a fine mesh, and shown in Figs. 7(c-f), are all within an acceptable range. The values of y+ are about two and four times larger for the medium and coarse meshes, respectively. The wall temperature on the solid surfaces for the PoF/ToF/He case is shown in Figs. 7(g-h). Cases PoG/ToF/He and PoF/ToF/He were chosen for the grid independence studies because they correspond to the lowest and highest values of the unit Reynolds numbers, respectively, for both air and helium streams (see Table 3). The hydrogen fuel stream has a larger value of the unit Reynolds number but because hydrogen is not currently used in the EIMP experiments, it was deemed important to explicitly evaluate the grid resolution requirements for the cases using the helium as a fuel simulant.

Contours of the Mach number, obtained from the simulations on the coarse, medium, and fine grids, on the z- and y-planes, for the two flow cases, PoG/ToF/He and PoF/ToF/He, are shown in Figs. 8-11. The z-planes are taken through the center-plane of the strut and ramp injectors. The y-planes are taken through the third fuel port counting from the bottom of the strut injector and the top fuel port of the ramp injector. Only near fields are shown on the y-planes to more clearly illustrate the cross-stream flow features. The key flow features such as shock waves, and flow compressions and expansions are qualitatively similar on all grids for each injector geometry and individual cases. As expected, the shock features get progressively refined as the grid resolution increases. For cases, PoG/ToF/He, which correspond to the lower values of the unit Reynolds number, the shock wave reflections dissipate much sooner downstream. The lower value of the Reynolds number is also evident by the increase in the shock-induced boundary layer separation that occurs on the side walls of the strut body.

The one-dimensional values of the total pressure recovery and the mixing efficiency versus the downstream distance in inches obtained from the simulations on the coarse, medium, and fine meshes are shown in Fig. 12. Due to the limitation of the one-dimensional post-processor to analyze only axial planes of data, these plots contain gaps where the complicated grid topology contained streamwise grid "wraps". The regions around each injector body, where grid "wraps" are present are shown in Figs. 5 and 6. Necessarily, those regions were omitted from the one-dimensional analysis.

The trends of the one-dimensional values of the total pressure recovery and the mixing efficiency change monotonically with increasing grid resolution. However, the rate of convergence at which these values approach their asymptotic state varies among the cases and with the downstream distance. This behavior is possibly due to the use of wall matching functions on the injector bodies. The behavior of these functions and the resulting boundary layers change for different grid densities as the y+ values change. To verify this claim another simulation was setup for the PoF/ToF/He case with the strut injector, where the solution upstream of the injection plane from the fine mesh simulation was interpolated onto the medium and coarse meshes and frozen such that only regions downstream of the injection plane were computed on the medium and coarse meshes. This simulation produced one-dimensional values of the total pressure recovery and the mixing efficiency much more consistent with convergence expectations for simulations approaching their asymptotic convergence state. However, because typical grid convergence studies generally do not include such interpolation procedures, the results obtained from the most common approach, where complete simulations on grids of different sizes are performed, are presented here. Another approach toward grid independence studies for flows with walls that could address the above issues would be to generate meshes with identical near-wall resolutions that become coarser only away from the walls. This way, the near-wall flows, that have the potential to impact the downstream flow features would be treated consistently among the simulations. This approach was not followed in the current simulations.

Because the unit Reynolds number is significantly lower for the case PoG/ToF/He, this case exhibits less variations in both quantities due to grid resolution. The higher unit Reynolds number case, PoF/ToF/He, exhibits more variations among the values. The differences between the values obtained on the coarse and medium meshes are generally larger than those found between medium and fine meshes. The error bars corresponding to the data obtained on the fine mesh and shown in Fig. 12 were obtained assuming a unity order of accuracy and using the Grid Convergence Index (GCI),[30] which is based on Richardson extrapolation. Although the formal order of accuracy of VULCAN-CFD is second order, unity order of accuracy was used for the GCI to ensure a conservative estimate of the errors. Furthermore, visual inspection of the differences between the one-dimensional values of the mixing efficiency, obtained from the simulations on
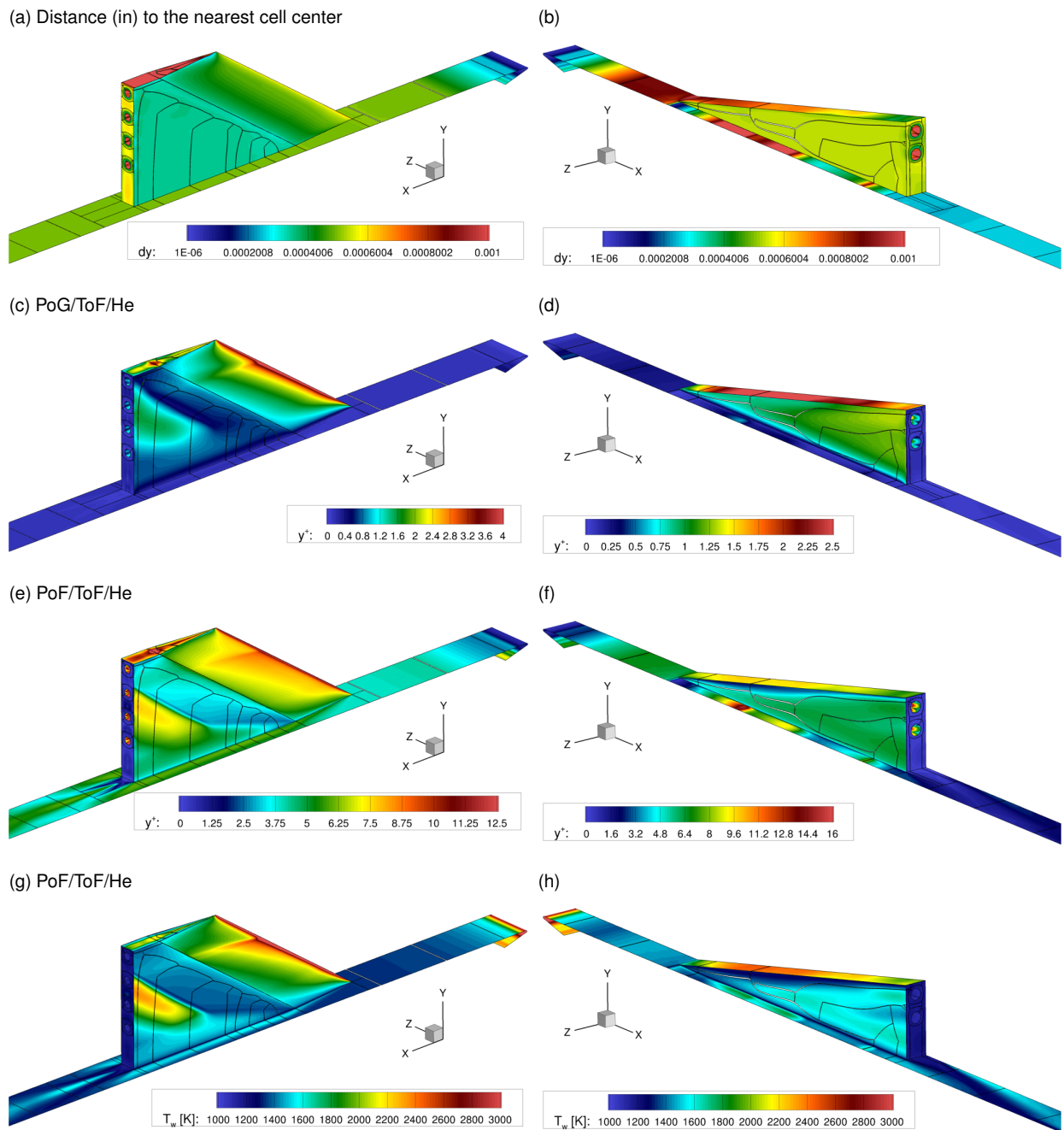
(a) Distance (in) to the nearest cell center

(b)

(c) PoG/ToF/He

(d)

(e) PoF/ToF/He

(f)

(g) PoF/ToF/He

(h)

Figure 7: Contours of the distance to the nearest cell center, y+ values for the PoG/ToF/He and PoF/ToF/He cases, and the wall temperatures, obtained for the fine grids for the strut (left column) and ramp (right column) simulations. The same values on medium and coarse meshes are about double, and quadruple, respectively, as those shown here.
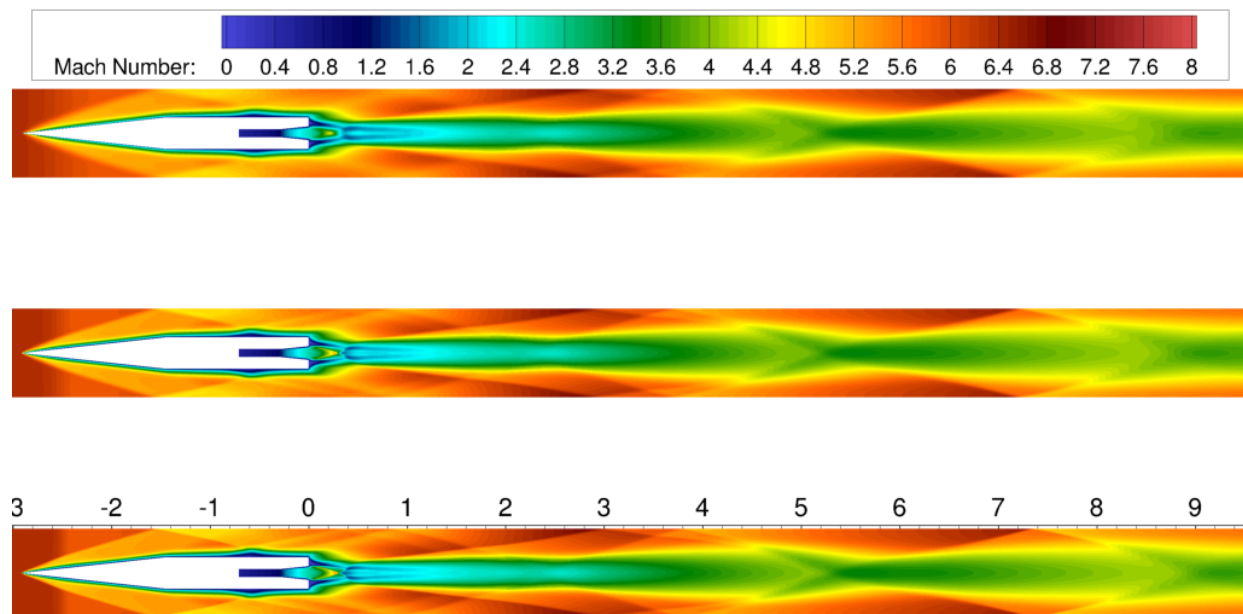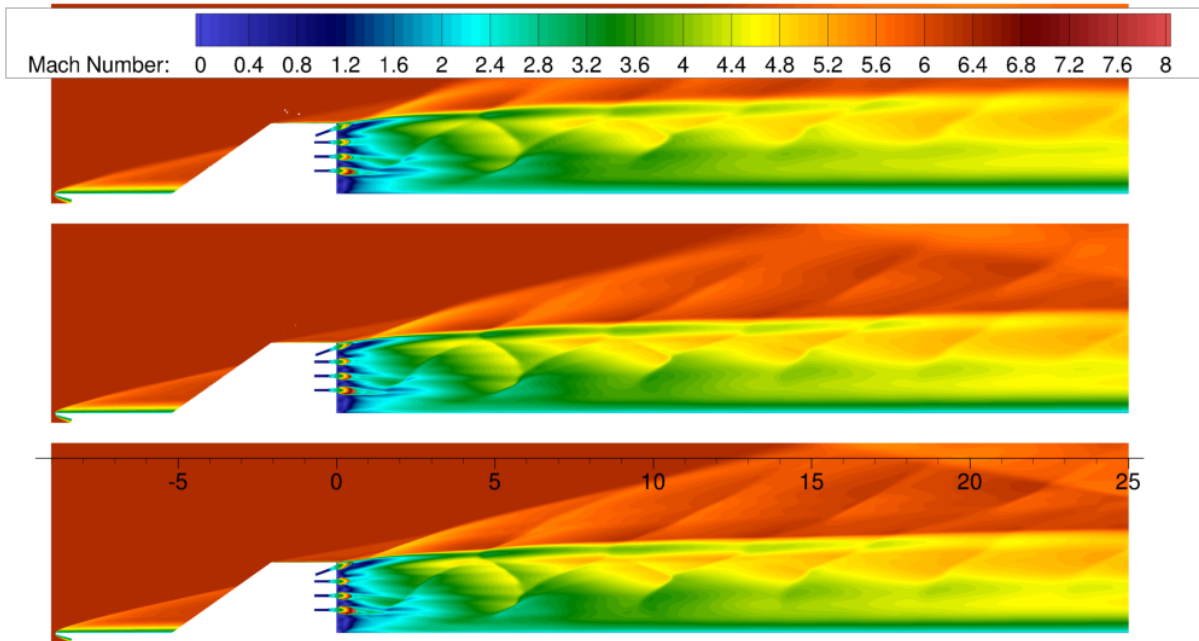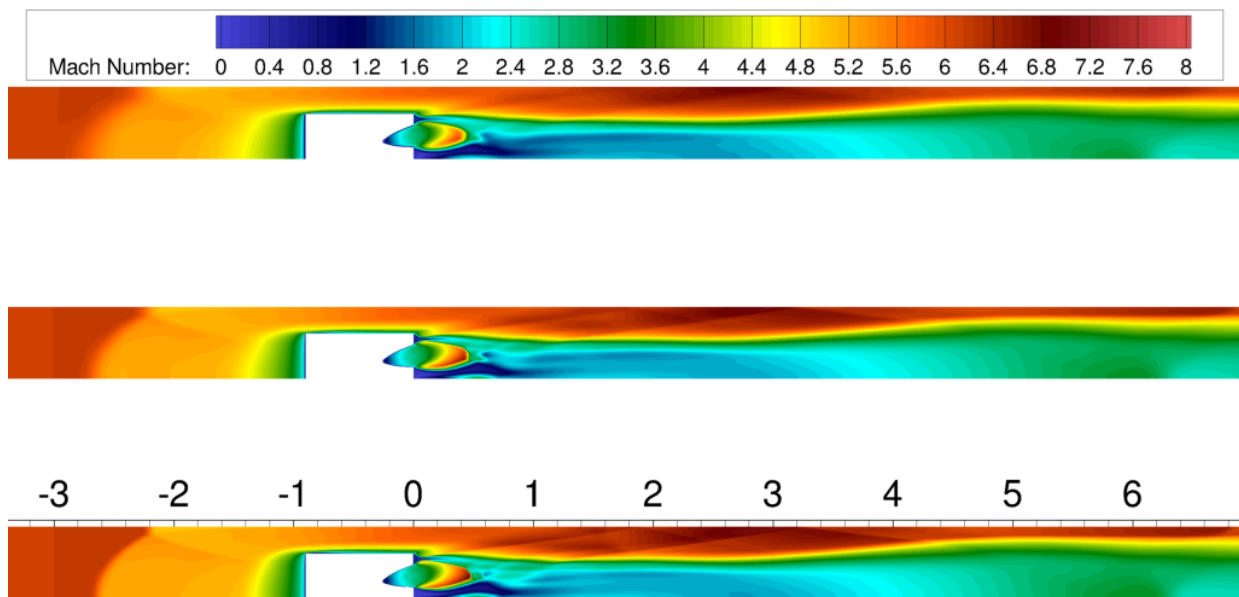
(a) z=0.0 in
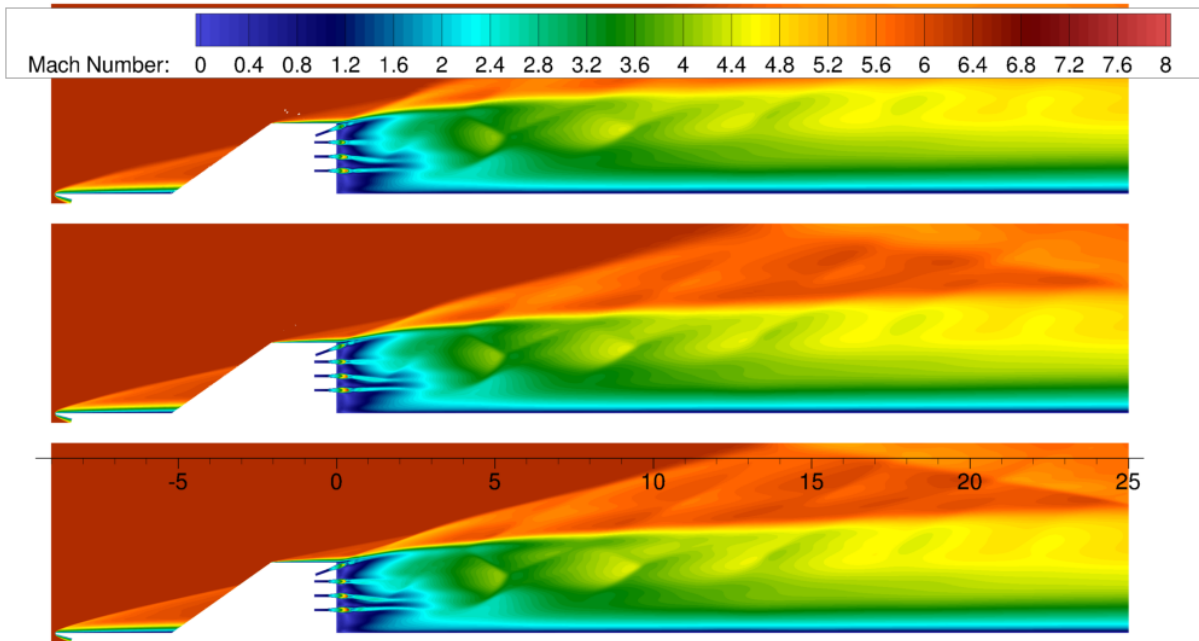
(b) y=1.6187 in

Figure 8: Contours of the Mach number on the (a) z-planes obtained through the center of fuel ports, and (b) y-planes obtained through the center of the third fuel port from the bottom for the strut injector simulations for case PoG/ToF/He on the coarse (top), medium (middle), fine (bottom) grids. Downstream distance is in inches.

(a) z=0.0 in

(b) y=1.6187 in
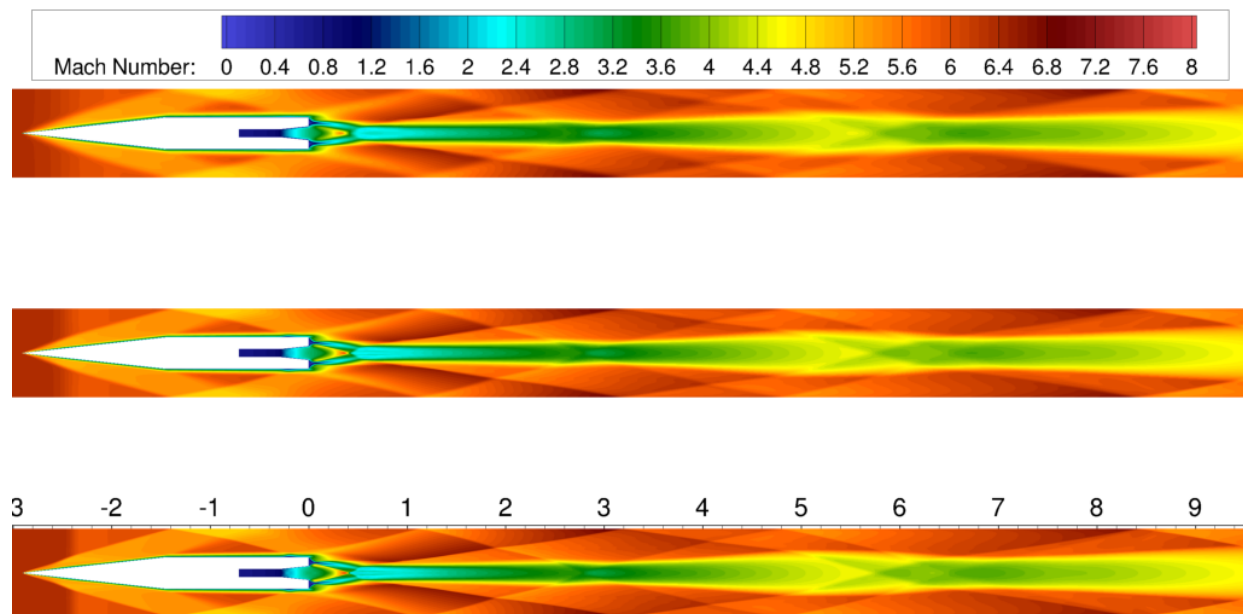
Figure 9: Contours of the Mach number on the (a) z-planes obtained through the center of fuel ports, and (b) y-planes obtained through the center of the third fuel port from the bottom for the strut injector simulations for case PoF/ToF/He on the coarse (top), medium (middle), fine (bottom) grids. Downstream distance is in inches.

(a) z=0.1875 in
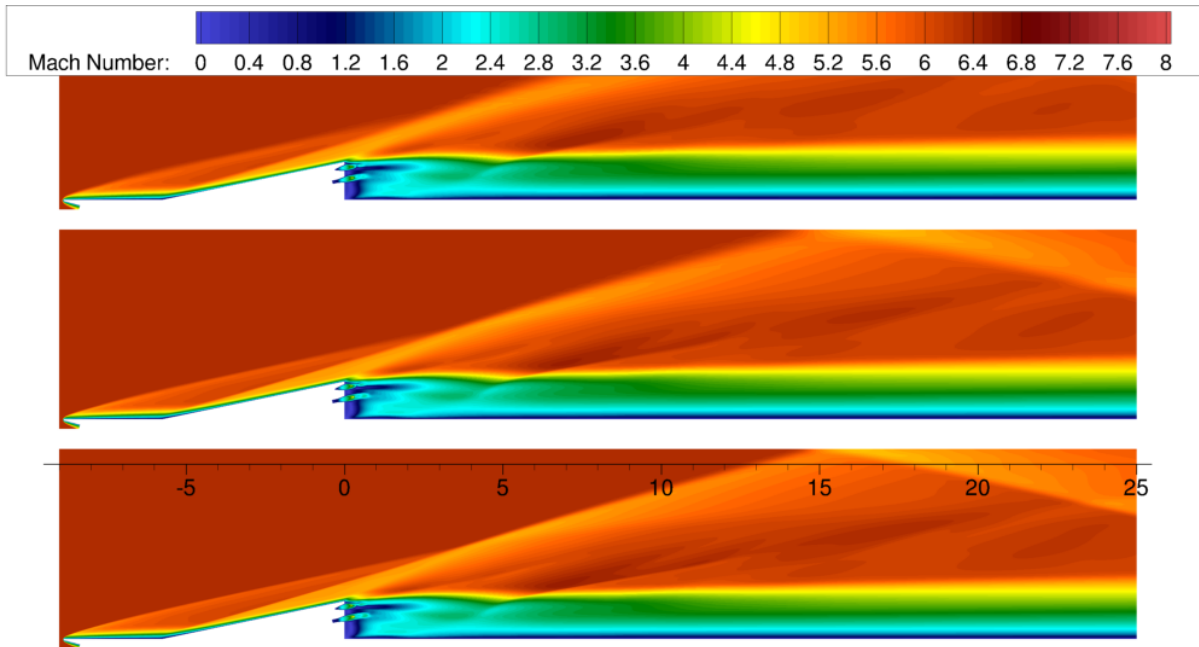
(b) y=1.0125 in
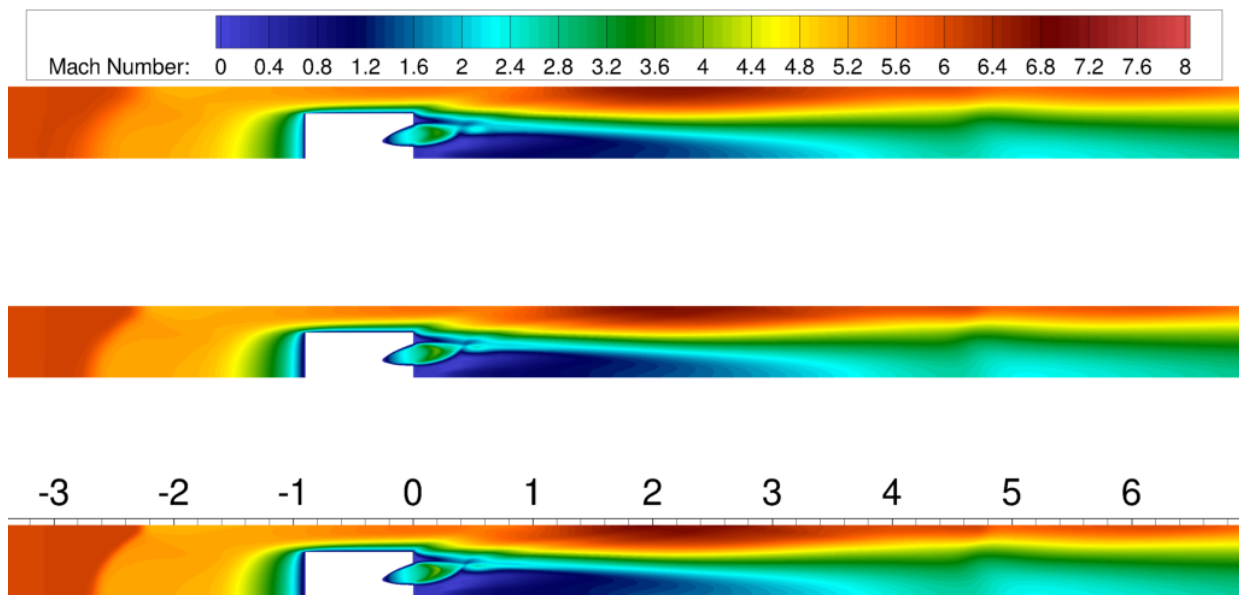
Figure 10: Contours of the Mach number on the (a) z-planes obtained through the center of fuel ports, and (b) y-planes obtained through the center of the top fuel port for the ramp injector simulations for case PoG/ToF/He on the coarse (top), medium (middle), fine (bottom) grids. Downstream distance is in inches.

(a) z=0.1875 in
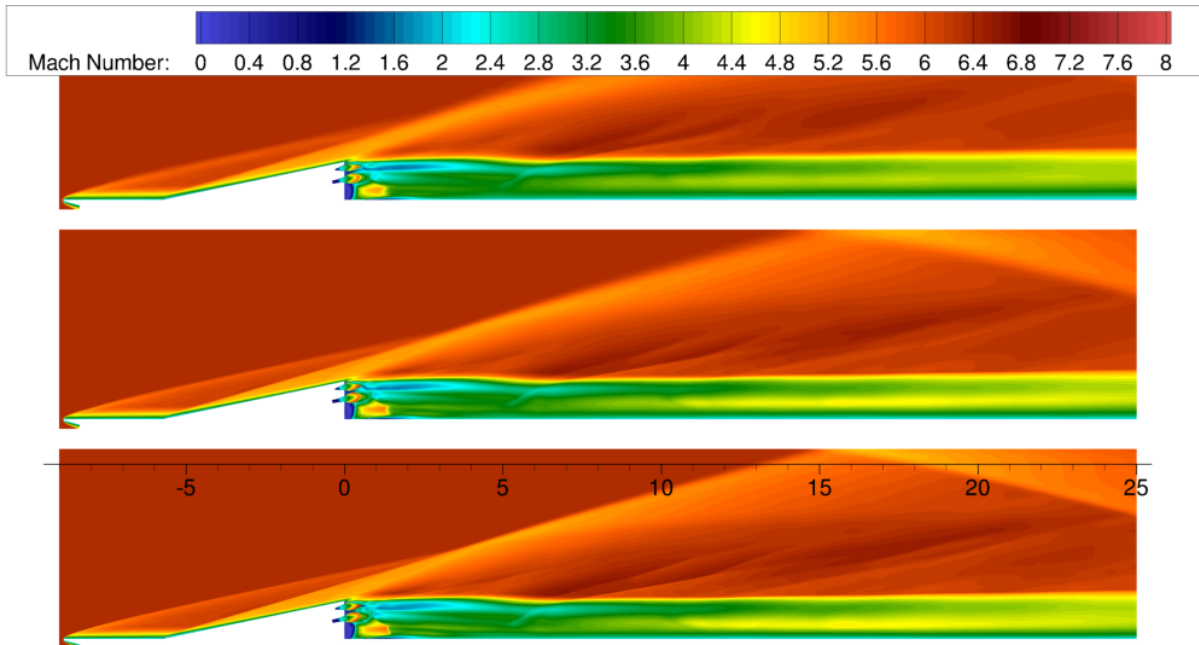
(b) y=1.0125 in

Figure 11: Contours of the Mach number on the (a) z-planes obtained through the center of fuel ports, and (b) y-planes obtained through the center of the top fuel port for the ramp injector simulations for case PoF/ToF/He on the coarse (top), medium (middle), fine (bottom) grids. The error bars for the fine mesh results were obtained using the GCI. Downstream distance is in inches.

the three different grids, reveals that these data appear to be converging slower than the formal order of accuracy of the solver. It should be noted that this result is not a reflection of the formal order of accuracy of the VULCAN-CFD solver, and is strongly impacted by the presence of shocks throughout the flow field. To ensure simulation stability, the solver reverts to the unity order of accuracy near these discontinuities. Effectively, the resulting error bars are proportional to the difference between the results obtained on the fine and medium meshes, and represent an estimate of the error bounds between the current result and its fully grid-converged value. The observed errors in the values of the total pressure recovery have a maximum value of about 5%, with 1-2% typical, and a maximum value of about 15% (in the near-field of the PoF/ToF/He ramp injector case) with 5% typical for the mixing efficiency. Because the errors in the 1D values of the quantities of interest approach limits typically encountered in the engineering analysis, only the results of the simulations obtained on the fine meshes are presented in the subsequent sections.

All of the current simulations were performed on the Pleiades Supercomputer located at NASA Ames. The computational cost associated with solving a single simulations on the fine mesh was about 60 k cpu hours. Simulations, were typically performed using 480 compute cores with most cases converging in 5 days. The total computational cost of the study was about 1 million CPU hours, which included medium and coarse mesh simulations (about 100 k CPU hours), and pre- and post-processing of the fine mesh simulation results (about 100 k CPU hours).

RESULTS AND DISCUSSION

Contour plots of the Mach number in the z-planes obtained through the center of the injector ports and midway between the injectors, and x-planes at various locations for the strut and ramp injectors for all of the cases are shown in Figs. 13-22. The flow is left-to-right. For the x-planes, the aspect ratio is not one because these planes are viewed looking aft-to-fore from an angle of about 30 degrees to the x-axis in the xz-plane. The streamwise distance on these figures is in inches. The Mach number contours are a convenient quantity to consider for the comparisons among the cases because the value of the Mach number at the inflow is the same for all the cases, while other quantities may vary. Furthermore, the value of the Mach number is impacted by changes in the local mixture composition (i.e., mixing) and heat release (for reacting cases), thereby allowing comparative visualization of such effects for all cases. The black isocontour line denotes the stoichiometric value of the hydrogen mass fraction, which closely approximates the location of the peak heat release in reacting flows and further delineates a boundary of our mixing metric of interest (Eq. (5)). The extent of mixing may be qualitatively discussed by visually examining the extent of the area enclosed by this isocontour line. However, some care should be exercised when interpreting this area because the fuel will diffuse to its stoichiometric isocontour value only in the global sense (and after long-time mixing or in the far-field). As the fuel and air mix in the near-field of the injector, there could exist local mixing regions where the equivalence ratio is rich or lean. In the former, the area enclosed by the stoichiometric value will simply grow more slowly, but in the latter case this area will first grow and then shrink and collapse as the fuel mixes with air to sub-stoichiometric proportions.

Qualitatively, the flow features for all of the cases for the strut and ramp injectors, respectively, are very similar. Upstream of the injector bodies, the leading edge of the flat plate causes a shallow bow shock at about 12.5 degrees to the flat plate, which is slightly larger than a Mach wave angle of about 9 degrees for this Mach number. The approach boundary layer thickness is comparable for all of the cases but somewhat larger for the PoG/ToG/He and PoG/ToF/He cases. In the former case, the flat plate wall is treated adiabatically, therefore, the temperature in the boundary layer corresponds to the adiabatic recovery temperature, which is about 850 K, the heating of the boundary layers has a tendency to thicken it. In the latter case, the flat plate is cooled to a temperature of about 1200 K, but the unit Reynolds number of the free stream air is two orders of magnitude lower than all the other cases. Since the boundary layer thickness is inversely proportional to the streamwise Reynolds number raised to, typically, some small power,[31] as the Reynolds number decreases, the boundary layer thickens and vice versa. Nevertheless, for all cases, the approach boundary layer is a fraction of the height of both the strut and the ramp injector bodies such that the side
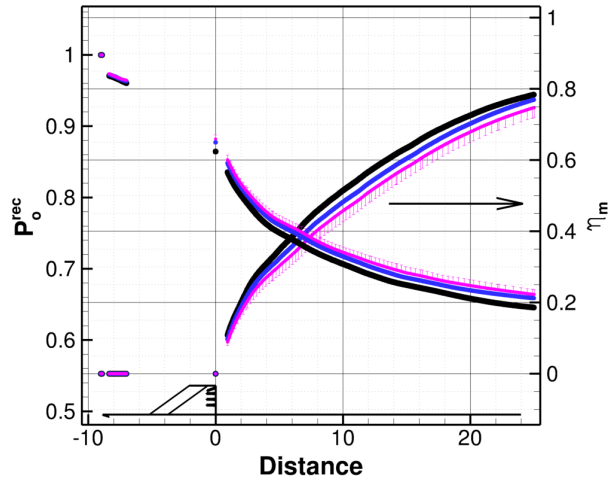
(a) PoG/ToF/He, Strut
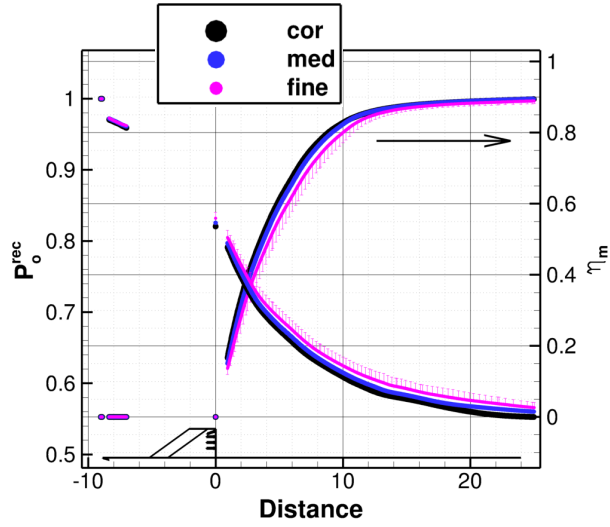
(b) PoG/ToF/He, Ramp
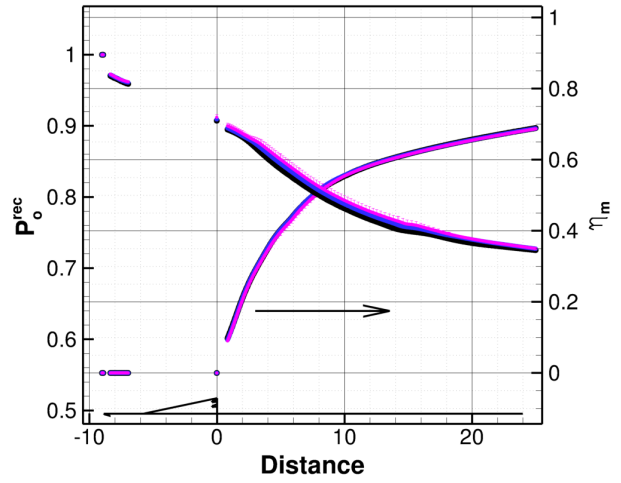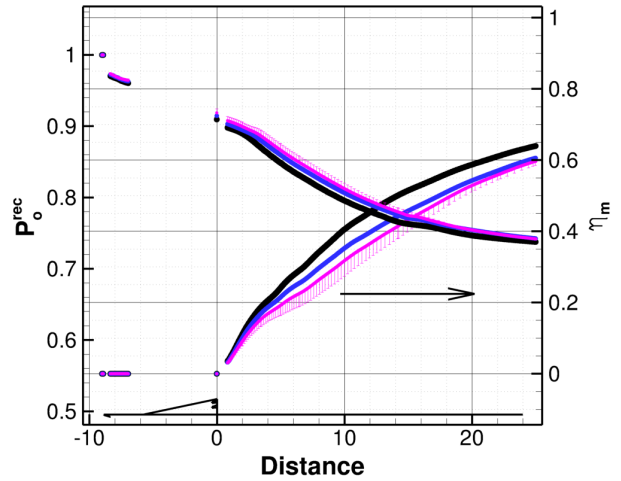
(c) PoF/ToF/He, Strut

(d) PoF/ToF/He, Ramp

Figure 12: one-dimensional values of the total pressure recovery and mixing efficiency vs. downstream distance (in inches) obtained from the simulations on the coarse, medium, and fine grids, for the cases corresponding to the smallest (PoG/ToF/He) and larges (PoF/ToF/He) values of the unit Reynolds number.
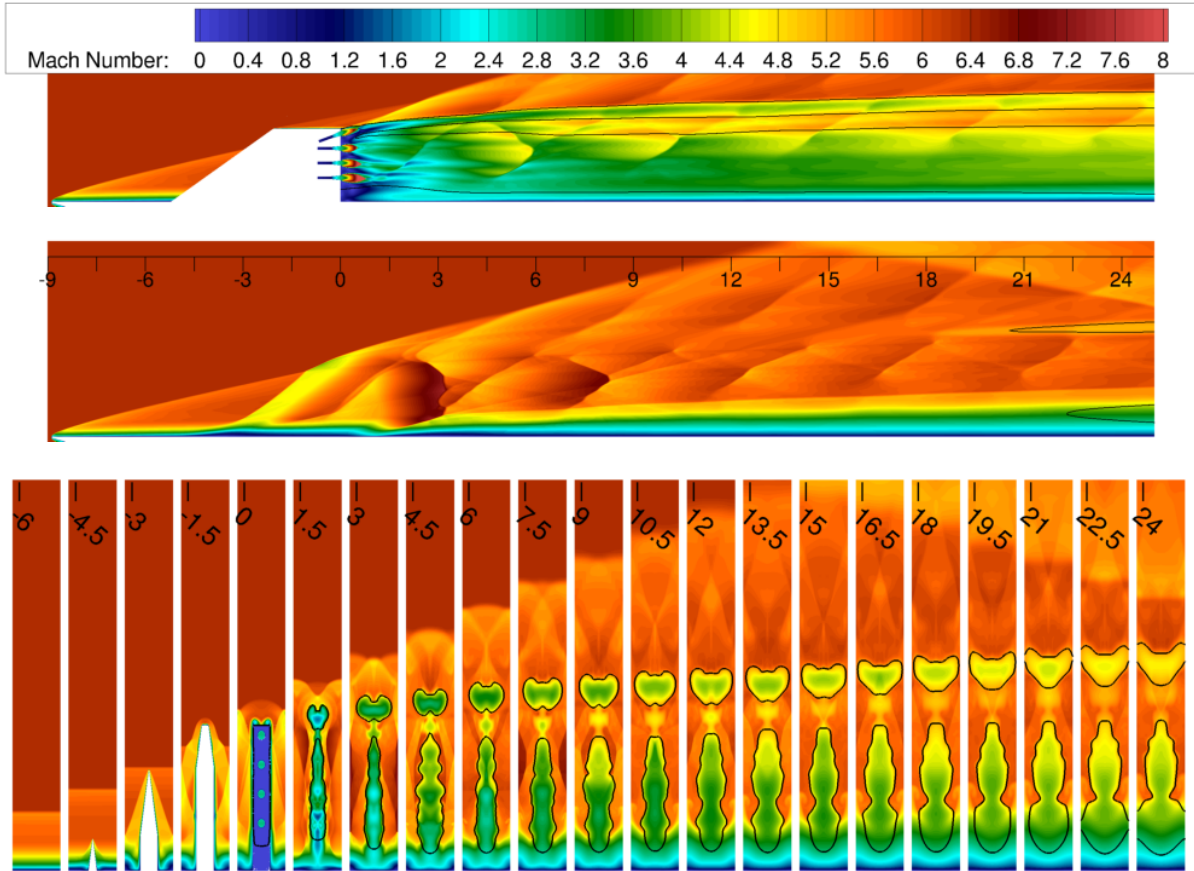
Figure 13: Contours of the Mach number on the z-planes obtained at the centerline, and half-way between the injectors, and x-planes at various downstream locations for the strut injector simulations for case PoG/ToG/He. Downstream distance is in inches. Black lines denotes the stoichiometric value of the fuel mass fraction.

walls of both injectors are exposed to the free stream air flow. As a consequence, the boundary layers that develop on the sides of the injector bodies, just as the boundary layer near the leading edge of the flat plate, are thin and transitional, which makes them more susceptible to shock-induced separation. For the current turbulence model, the transition is expected to occur at a streamwise Reynolds number that is about an order of magnitude lower than that found in most turbulent flows of engineering interest.[29] Therefore, the simulated flows are expected to become fully turbulent sooner than their realistic counterparts and will, therefore, be more resilient to shock-induced separation.

For the strut injector cases, shown in Figs. 13-17, a cross-stream shock wave is generated by the sharp leading edge of the strut injector body (e.g., x=-3). The turning half-angle of the strut injector body leading edge is 6.25 degrees (see Fig. 3), resulting in the leading edge shock wave angle of about 17 degrees. Because the leading edge of the strut body is swept at 35.4 degrees, the resulting oblique shock wave is also swept back at the same angle. This shock wave propagates in the cross-stream direction and impacts the body of the adjacent injector. This propagation is evident by the change in the value of the Mach number at downstream locations between -3 and 0 inches on the middle plots of each figure. The impact of this oblique shock on the body-side of the injector is also evident by the increase in the value of the y+ and the wall temperature seen previously on Figs. 7(c),(e), and (g). After the body-side reflection, the oblique shock waves continue to pass through one another and interact, leading to a complex downstream pattern seen in the figures. As these shock waves pass through the variable density fuel-air interface, vorticity is
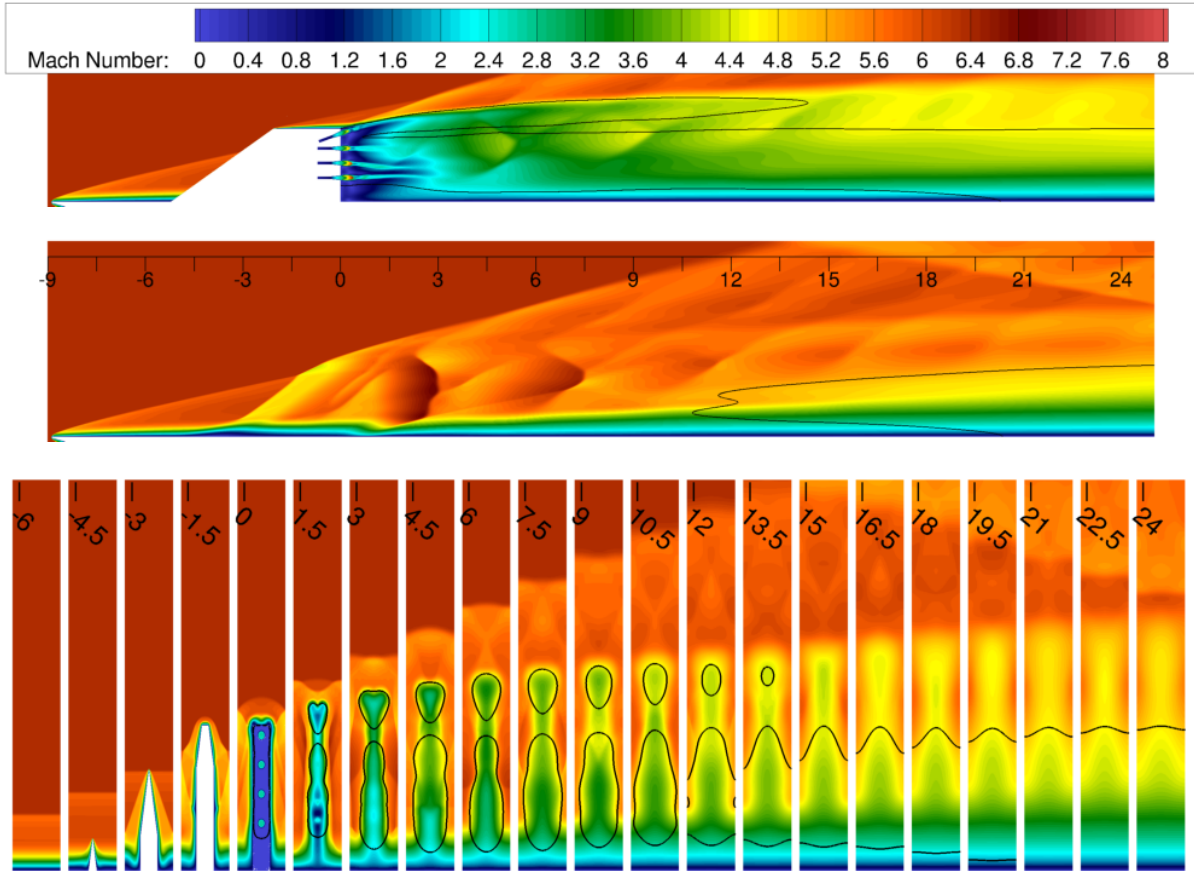
Figure 14: Contours of the Mach number on the z-planes obtained at the centerline, and half-way between the injectors, and x-planes at various downstream locations for the strut injector simulations for case PoG/ToF/He. Downstream distance is in inches. Black lines denotes the stoichiometric value of the fuel mass fraction.

produced locally due to the effect of the baroclinic torque. While the baroclinic effects are generally small, this vorticity curves and stretches the local fuel-air interface regions, thereby increasing the fuel-air mixing rate, albeit at the expense of total pressure losses. As the flow continues past the strut injector body, a counter rotating vortex pair (CVP) forms near the tip of the injector body. The top-most fuel port injects the fuel stream directly at the space between the CVP. The combined effect of the angled injection and the CVP distorts and bifurcates the top-most fuel stream, and separates it from those of the three lower parallel fuel ports. This effect can be seen by observing the stoichiometric value of the mass fraction as it evolves in the x-planes in Figs. 13-17 for all cases.

For the ramp injector cases, shown in Figs. 18-22, an oblique shock wave is generated by the inclined ramp surface of the ramp injector body. The turning angle of the ramp surface is 11.8 degrees (see Fig. 4), resulting in the oblique shock wave angle of about 16 degrees at the injector centerline. This oblique shock interacts and joins with the same shock wave produced by the adjacent injector bodies. However, unlike the cross stream shock waves that emanate from the leading edge of the strut, the ramp body oblique shock wave does not interact with the fuel-air mixing plume but instead serves primarily to introduce a pressure difference between the top of the ramp surface and the gap between the adjacent injectors. The pressure is higher on the ramp surface, which creates a driving force for the flow to spill from the ramp surface into the gap between the adjacent injectors. This spillage introduces counter rotating vortices on either side of the ramp injector body with the size proportional to the ramp height. These vortices are large compared to the
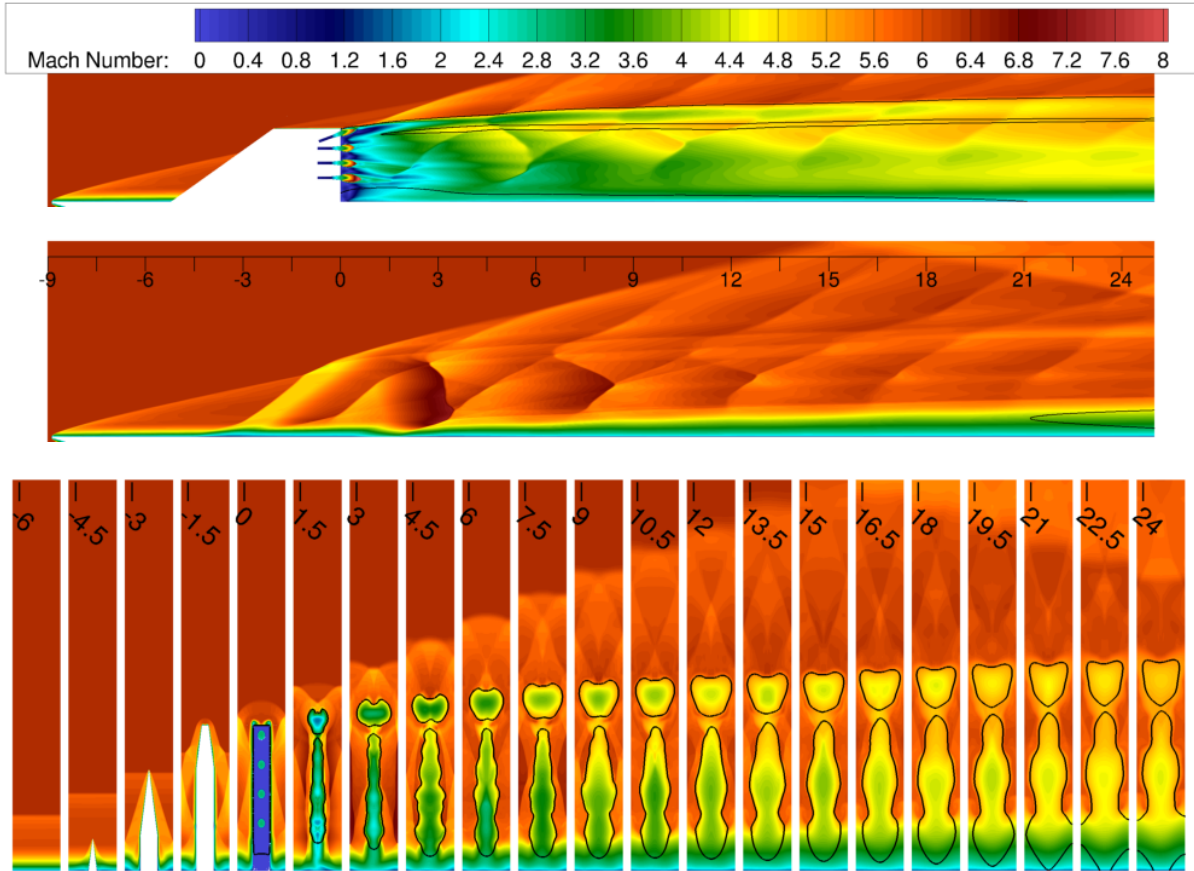
Figure 15: Contours of the Mach number on the z-planes obtained at the centerline, and half-way between the injectors, and x-planes at various downstream locations for the strut injector simulations for case PoF/ToF/He. Downstream distance is in inches. Black lines denotes the stoichiometric value of the fuel mass fraction.

size of the fuel ports. Therefore, when they begin to interact with the injected fuel streams, they stretch and push the fuel-air interface away from the boundary layer and up into the core of the flow. This process is further aided by the fact that all the ramp fuel ports are angled at 11.8 degrees up and the top set is angled at 10 degrees outwards towards the gap between the adjacent injectors. The combined effect of the angled injection and the large-scale CVP spreads the fuel through the intended fueling area. These effects can be seen by observing the stoichiometric value of the mass fraction as it evolves in the x-planes in Figs. 18-22 for all cases.

The impact of the total enthalpy can be investigated by examining results corresponding to cases PoG/ToG/He and PoG/ToF/He, corresponding to the "cold" flow and true flight enthalpy, respectively, and shown in Figs. 13 and 14, and Figs. 18 and 19 for the strut and ramp injectors, respectively, both at the ground facility total pressure. The differences between the Mach number contours and the mixing (as quantified by the isocontours of stoichiometric value of fuel mass fraction) are significant. It appears that the PoG/ToF/He case diffuses and mixes the fuel streams much more rapidly than the PoG/ToG/He case for both injectors. This is evident by examining the isocontours of the stoichiometric value of the fuel mass fraction, which indicate that the fuel diffuses toward the gap between adjacent injectors and into the core flow and the boundary layer much more rapidly for the high enthalpy case. Despite the value of the Mach number being the same for all cases, the velocity of the free stream air for the high enthalpy case is over three times that of the "cold" flow simulation, while the velocities of the respective fuel streams are the same. This
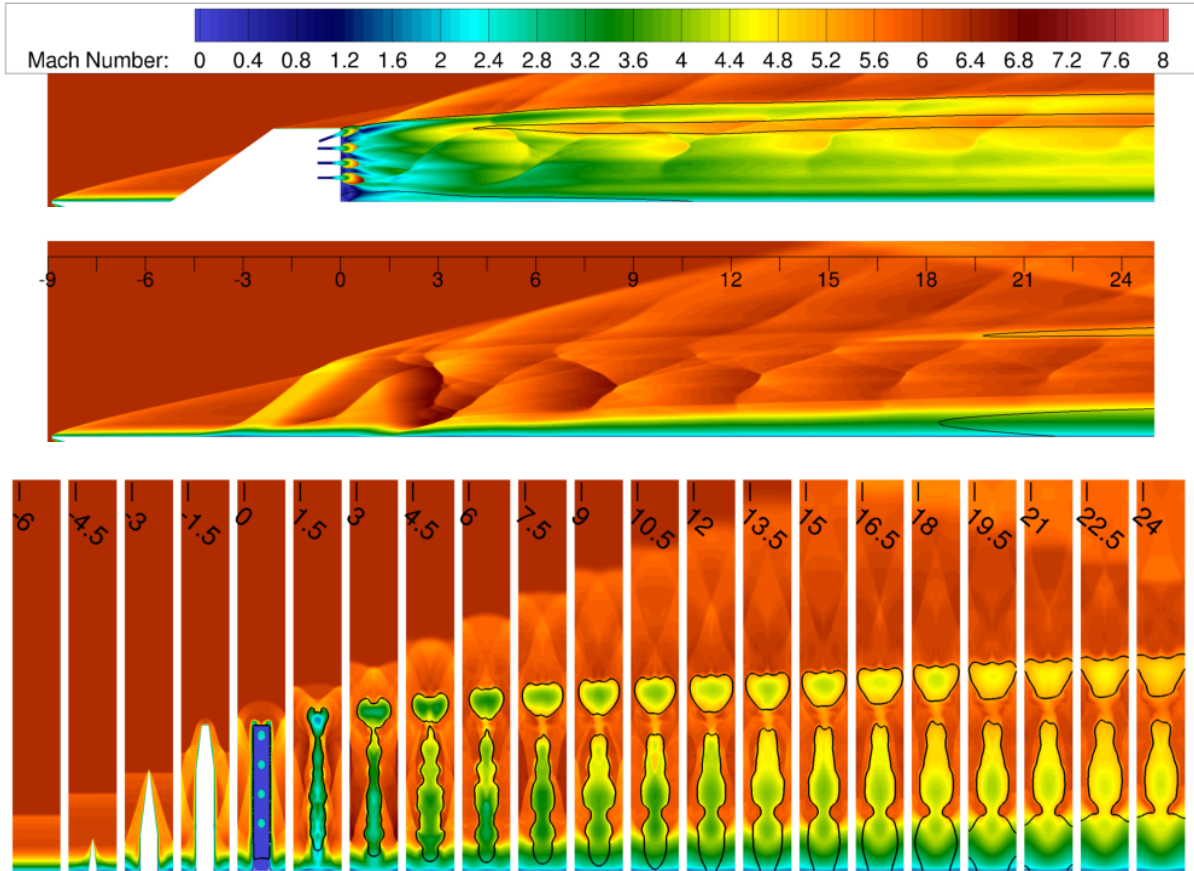
Figure 16: Contours of the Mach number on the z-planes obtained at the centerline, and half-way between the injectors, and x-planes at various downstream locations for the strut injector simulations for case PoF/ToF/H2. Downstream distance is in inches. Black lines denotes the stoichiometric value of the fuel mass fraction.

introduces a significantly greater shear between fuel and air streams for the high enthalpy case. This shear, when quantified in terms of the velocity difference parameter computed in Table 3, has been correlated with the increase in the shear layer growth rate by Brown and Roshko.[20] The same authors also correlated increasing value of the fuel-to-air stream density ratio with the further increase in the shear layer growth rate. While both correlations were found from work with planar compressible and incompressible mixing layers without strong shocks, Hussain and Husain[32] found close similarity between the characteristics of planar and axisymmetric mixing layers. Comparative assessment among all cases of both the velocity difference parameter and the fuel-to-air density ratio, does reveal that their values are the largest for the PoG/ToF/He case. However, Bogdanoff[21] and Papamoschou and Roshko[3] found that in similar canonical flows the increasing values of the convective Mach number suppress the shear layer growth rate. The value of this quantity is also the largest for the PoG/ToF/He case, nevertheless, despite the potential for suppression of mixing, it appears that the mixing enhancements due to the large values of the velocity difference parameter and the density ratio have a leading effect, at least for the current cases of interest. Further investigation is needed to assess the relative impact of these competing factors on the current simulations.

The impact of the change in the value of the total pressure from that in the ground facility to the flight is not evaluated in isolation (i.e., both total pressure and total temperature of helium are changed simultaneously between cases PoG/ToF/He and PoF/ToF/He). This is because the change in the total pressure would only scale the values of the mass flow rates of air and fuel from those corresponding to the PoG/ToF/He case to
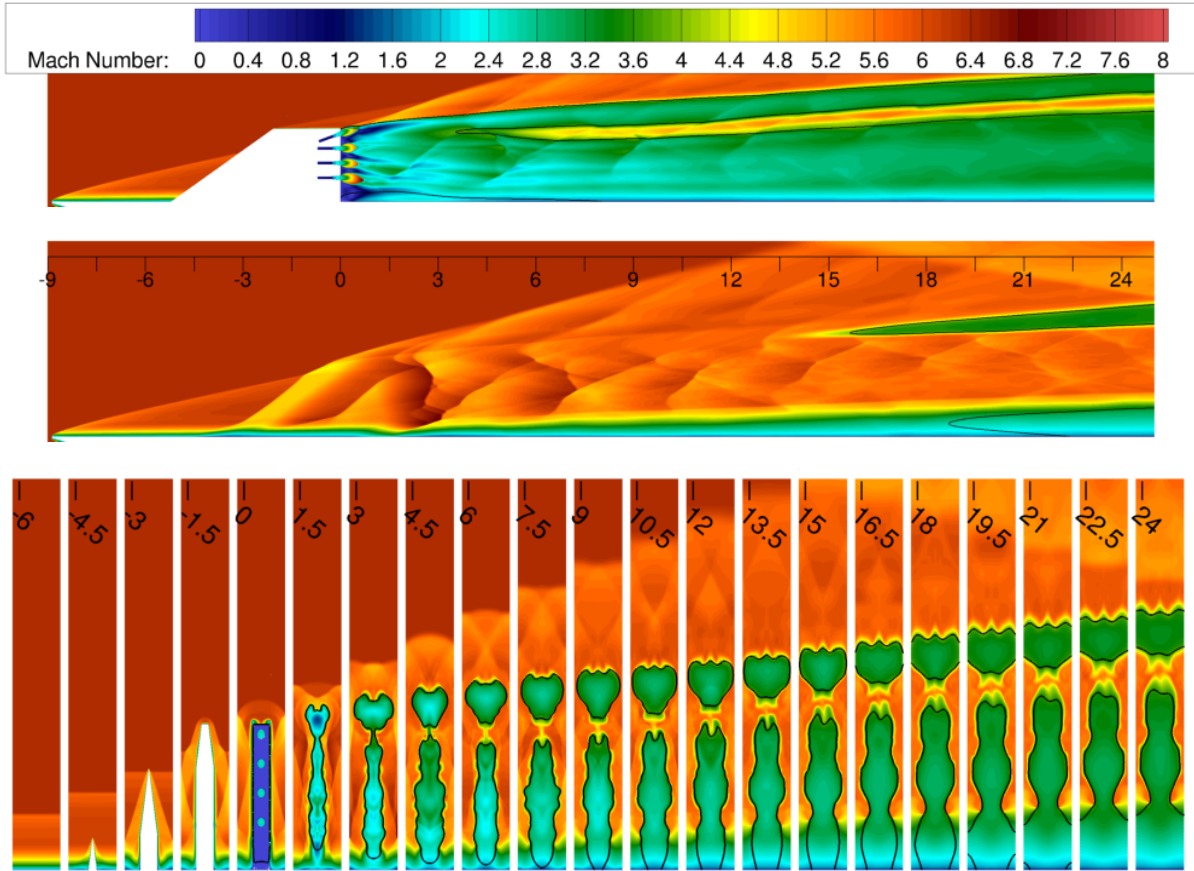
Figure 17: Contours of the Mach number on the z-planes obtained at the centerline, and half-way between the injectors, and x-planes at various downstream locations for the strut injector simulations for case PoF/ToF/H2/R. Downstream distance is in inches. Black lines denotes the stoichiometric value of the inert species mass fraction.

those being considered for the PoF/ToF/He case. Furthermore, without the change in the helium total temperature for the PoF/ToF/He case, all the metrics of interest to mixing (in Table 3 for the PoG/ToF/He case) would be the same between case PoG/ToF/He and this potential intermediate case. The unit Reynolds numbers would change to those comparable to the PoF/ToF/He case, nevertheless the mixing flow field was expected to closely resemble that for the PoG/ToF/He case. The impact of the isolated change in the value of the total pressure of the air can still be assessed upstream of the fuel injection plane by examining Figs. 8, 9, 14 and 15; and Figs. 10, 11, 19 and 20, for the strut and ramp injectors, respectively. This impact is most notable in the significant boundary layer separation that occurs on the body-side of the strut for the PoG/ToF/He case (see Fig. 8), which induces additional shocks and total pressure losses for that case.

The impact of the fuel simulant can be assessed by examining the results corresponding to cases PoF/ToF/He and PoF/ToF/H2, corresponding to the helium and hydrogen (non-reacting in the CFD), respectively, and shown in Figs. 15 and 16, and Figs. 20 and 21 for the strut and ramp injectors, respectively. Qualitatively, the contours of the Mach number are very similar. Close examination of the isocontours of the stoichiometric value of the hydrogen mass fraction for the PoF/ToF/He cases does reveal a slight increase in the spreading of the area contained within this isocontour as compared to the PoF/ToF/H2 cases. This can be observed by the decrease in the gap between the mixing plume from the upper port injector and lower three for the strut, or by the increased rate of spread into the boundary layer for the ramp. The cross-stream spreading
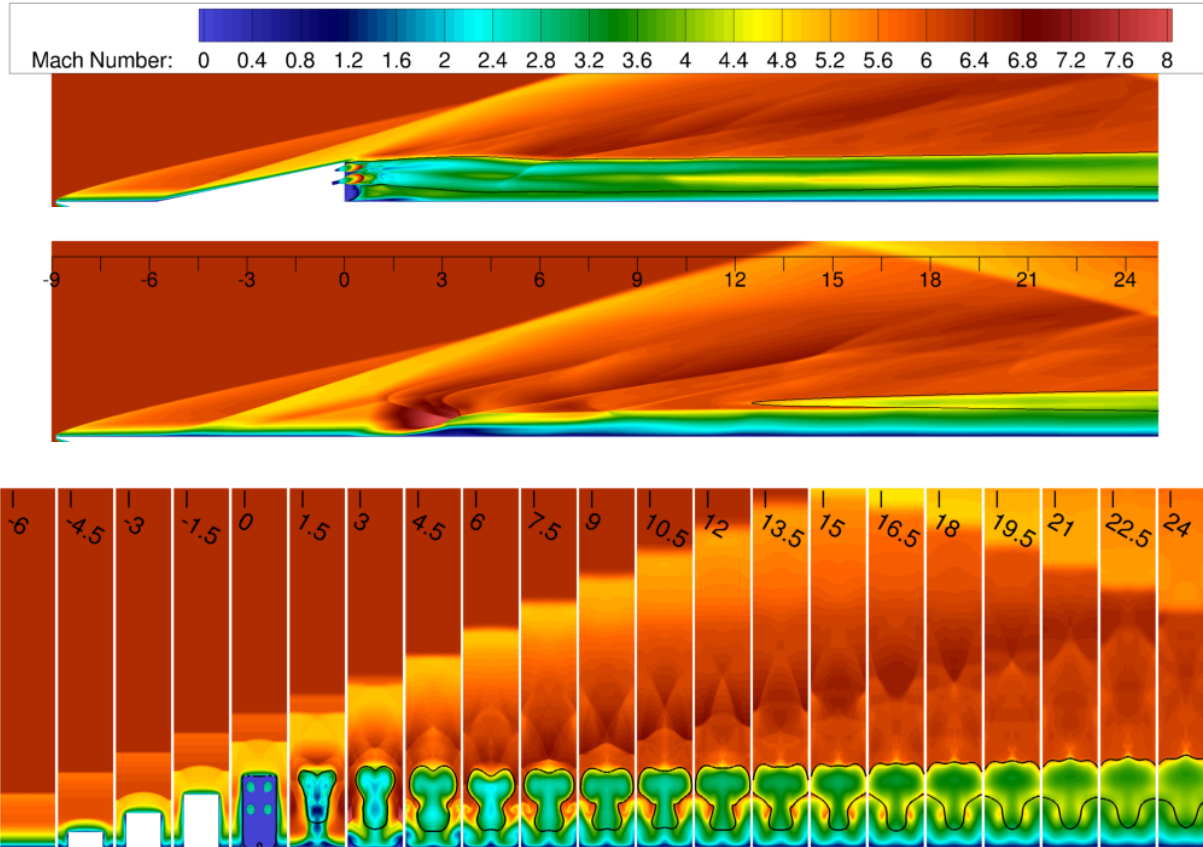
Figure 18: Contours of the Mach number on the z-planes obtained through the center of the injector ports, and half-way between the injectors, and x-planes at various downstream locations for the ramp injector simulations for case PoG/ToG/He. Downstream distance is in inches. Black lines denotes the stoichiometric value of the fuel mass fraction.

also appears slightly enhanced for the PoF/ToF/He cases for both injector bodies. The velocity difference parameter and the fuel-to-air density ratio are larger for the PoF/ToF/He case than for the PoF/ToF/H2 case, but again the convective Mach number is also larger. As discussed above, comparatively larger values of these quantities produce competing effects of enhancement and suppression of the mixing layer growth rates. Consistent with the case above, the velocity difference parameter and the density ratio seem to again play the leading role because the PoF/ToF/He case appears slightly more efficient than the PoF/ToF/H2 case at mixing the fuel and air streams. The small differences discussed here will be further quantified below by examining several one-dimensional metrics of interest for all of the cases.

The impact of the heat release can be investigated by examining the results from cases PoF/ToF/H2 and PoF/ToF/H2/R, corresponding to the non-reacting and reacting simulations, respectively, and shown in Figs. 16 and 17, and Figs. 21 and 22 for the strut and ramp injectors, respectively. First, as expected, for the reacting case, the value of the Mach number is visibly reduced inside the area enclosed by the iso-contour line, as the hydrogen and air mix, react, and release heat. However, it also appears that this area is significantly enlarged as compared to the non-reacting case. Whereas, in previous discussions of the non-reacting case where this effect was indicative of improved mixing, care must be taken when interpreting the results corresponding to the reacting case. This is because combustion is accompanied by a local increase in both the temperature and pressure. Although it is clear that combustion leads to local expansion for constant-pressure low-speed flows because the increase in the value of the temperature causes a
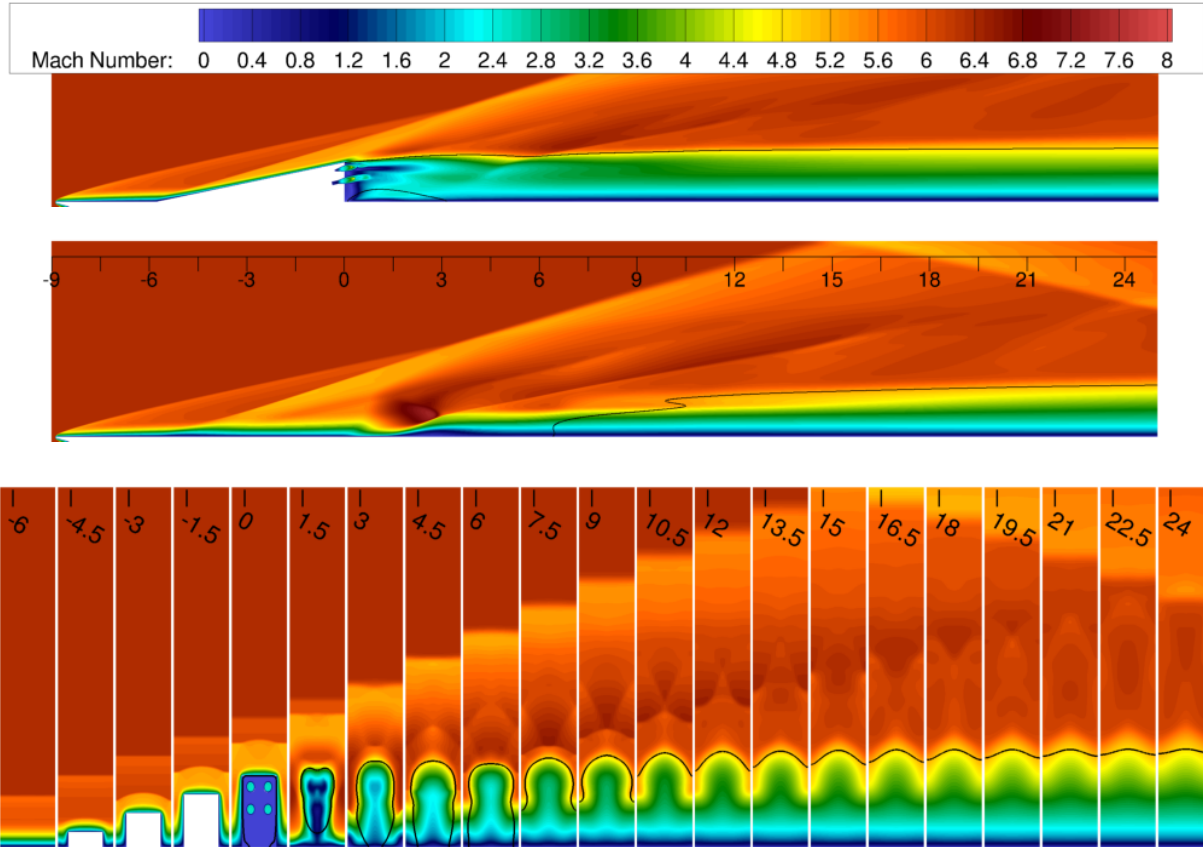
Figure 19: Contours of the Mach number on the z-planes obtained through the center of the injector ports, and half-way between the injectors, and x-planes at various downstream locations for the ramp injector simulations for case PoG/ToF/He. Downstream distance is in inches. Black lines denotes the stoichiometric value of the fuel mass fraction.

proportional decrease in the value of the density, simple analysis of the canonical Rayleigh flow reveals that in high-speed compressible flows, the flow actually contracts (i.e., density increases or specific volume decreases) when heat is added. Furthermore, molecular weight of the mixture increases when a combustion product, water, is introduced into the mixture, thereby further decreasing the specific volume. Nevertheless, examination of the values of the density (not shown) for the PoF/ToF/H2/R case reveals that they actually decrease as compared to the non-reacting, PoF/ToF/H2, case causing local expansion of the fuel-air mixing plume. This implies that the combustion processes under the current conditions behave more like the constant-pressure combustion than a Rayleigh flow with heat addition. Although this expansion causes an increase in the area enclosed by the stoichiometric value of the inert mass fraction, it is unclear whether a corresponding increase in the mixing is also present. Nevertheless, it does appear that the heat release enhances the core flow penetration of the fuel-air mixing plume for both strut and ramp injectors.

The plots of the one-dimensional values of the mass-flux-weighted average Mach number, mixing and combustion (for reacting cases) efficiency, total pressure recovery, and the specific thrust potential versus distance in inches are shown in Figs. 23 and 24 for the strut and ramp injectors, respectively. The injector body profiles are also shown with the injection plane denoted by zero. These plots help to quantify the overall behavior of the flow and the level of mixing and losses found among all of the simulated cases. Considering the one dimensional value of the Mach number first, the results indicate that the Mach number decreases throughout the flow. The decreases are caused by the leading effect of the shock and friction
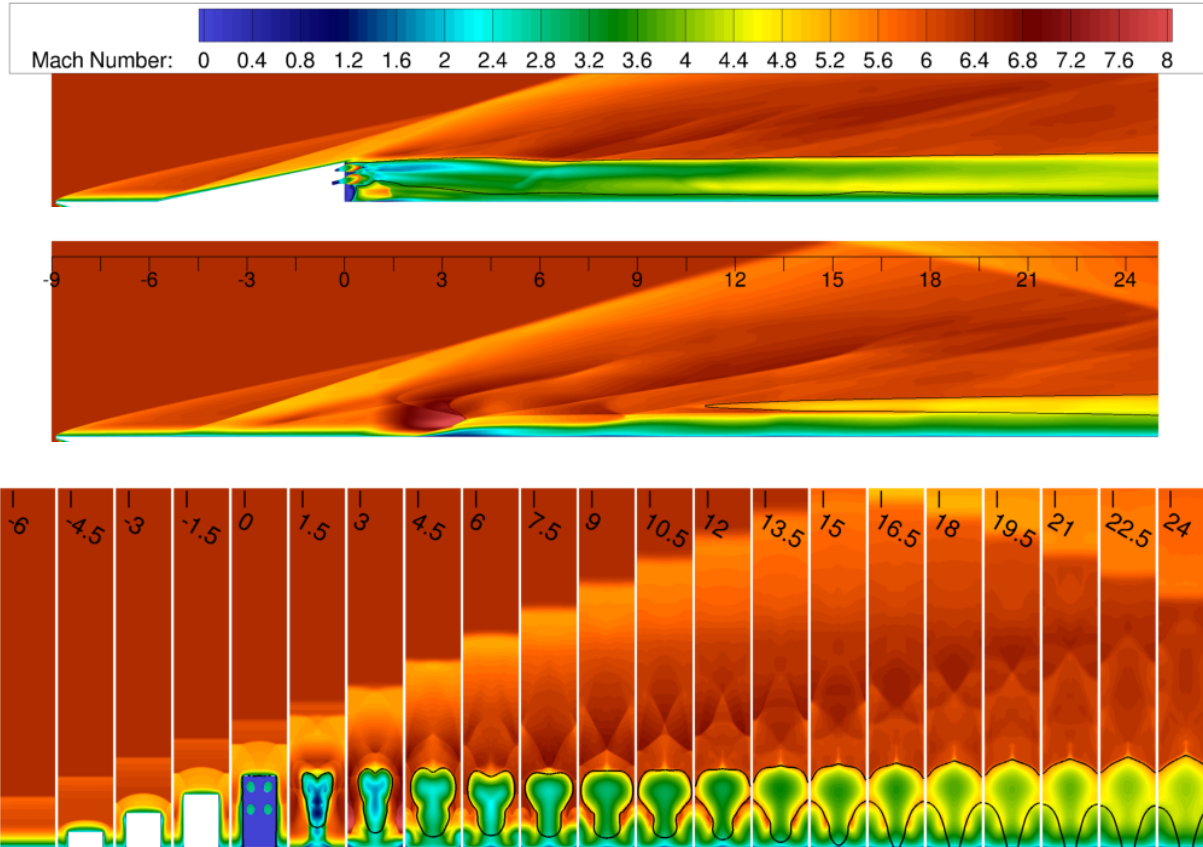
Figure 20: Contours of the Mach number on the z-planes obtained through the center of the injector ports, and half-way between the injectors, and x-planes at various downstream locations for the ramp injector simulations for case PoF/ToF/He. Downstream distance is in inches. Black lines denotes the stoichiometric value of the fuel mass fraction.

losses throughout the flowpath and the mixing losses downstream of the injection plane. The heat loss to the flat plate and injector bodies, which would tend to increase the value of the Mach number, appears to have a secondary effect. Downstream of the injection plane the profiles of the Mach number appear to follow a stair-stepping pattern. This effect is caused by the shock waves crossing through, reflecting, and interacting with the mixing plume and is more pronounced in the strut injector case. The value of the Mach number decreases more rapidly for the reacting cases due to heat addition by combustion processes.

The mixing efficiency results are consistent with the observations of the Mach number contours and the corresponding areas enclosed by the stoichiometric values of the fuel species elemental mass fractions. The fuel and air mix the fastest in the PoG/ToF/He case. The order with which mixing increases is well correlated with the values of the global velocity difference parameter shown in Table 3 for both ramp and strut cases, respectively. It is possible that a method could be devised to collapse all the mixing curves into one via this parameter or a combination of the other global parameters shown in the table. The mixing efficiency obtained from the reacting cases is lower that that obtained for the corresponding non-reacting cases indicating that combustion suppresses the mixing processes despite expanding the fuel-air mixing plume. The combustion efficiency based on the fuel depletion, denoted by the dotted line in the plots, supports the assertion that the heat release is added rapidly when chemical reactions are considered. This is because the values of the combustion efficiency are only slightly lower than those for the mixing curve. Finally, the mixing efficiency for the "cold" flow ground conditions (PoG/ToG/He), closely matches that for
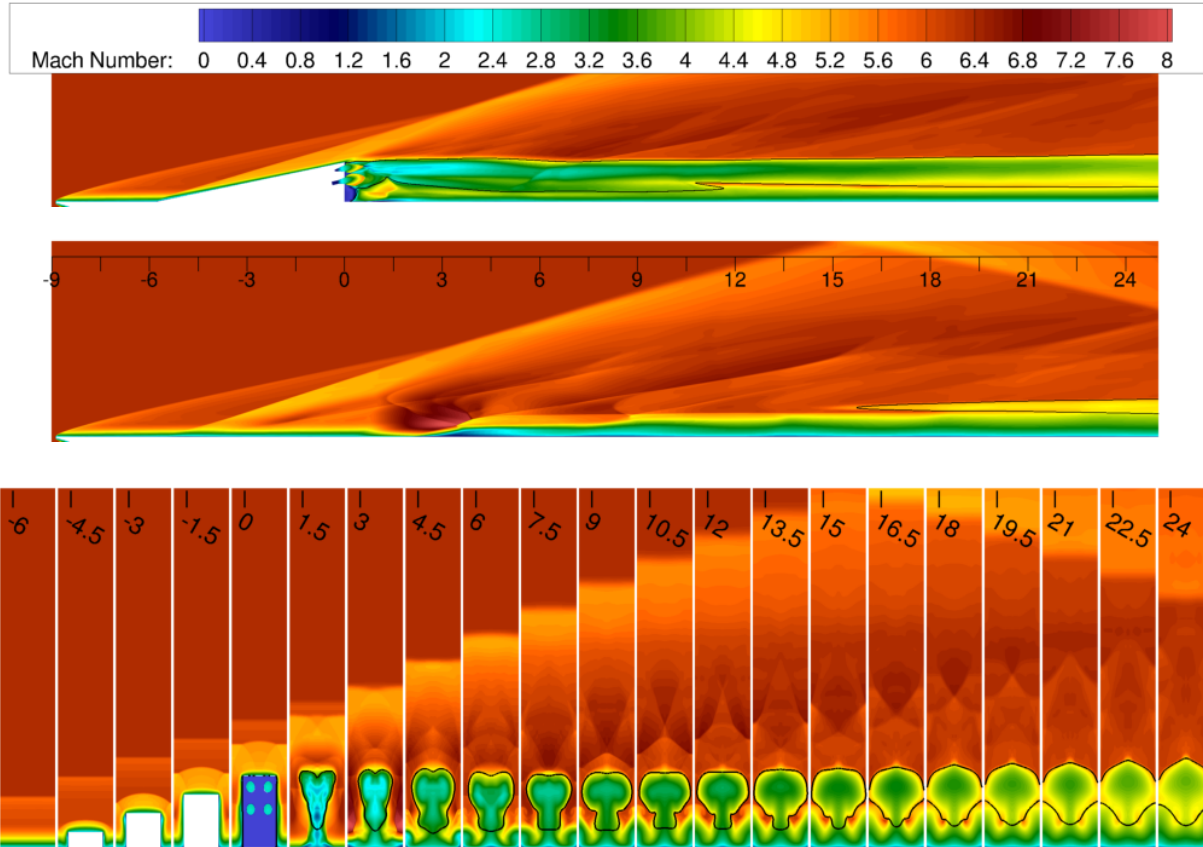
Figure 21: Contours of the Mach number on the z-planes obtained through the center of the injector ports, and half-way between the injectors, and x-planes at various downstream locations for the ramp injector simulations for case PoF/ToF/H2. Downstream distance is in inches. Black lines denotes the stoichiometric value of the fuel mass fraction.

the true flight conditions with hydrogen, with or without reactions (PoF/ToF/H2 and PoF/ToF/H2/R cases). But, the ground simulations with the true flight enthalpy (PoG/ToF/He) are the furthest from their intended flight condition.

The total pressure recovery profiles show an expected trend. Because the total pressure is proportional to the entropy, the total pressure recovery can only decrease. The decreases are due to shock and viscous losses upstream of the injection plane and also mixing and combustion downstream. About 8%-16% of the total pressure losses occur upstream of the injection plane with the strut body inducing almost twice as much losses as the ramp. Downstream of the injection plane, the mixing and combustion losses further contribute to the decrease. The losses due to combustion can be evaluated by comparing cases PoF/ToF/H2 and PoF/ToF/H2/R. For the current conditions, total pressure losses due to chemical reaction processes are about 5% and 1% for the strut and ramp, respectively. In general, the losses are inversely proportional to both mixing and heat release, i.e., greater mixing and heat release induce more total pressure losses. Cases PoG/ToG/He and PoF/ToF/H2 for the strut injector appear to be the exception to this generalization because case PoF/ToF/H2 exhibits less total pressure loss yet has a higher mixing efficiency as compared to the PoG/ToG/He case. However, this result should be kept in perspective because the total pressure recovery is a normalized quantity and represents a fraction of its reference value not the absolute amount of loss incurred. It is possible that under drastically different static flow conditions, the fraction of the total pressure required to mix the flow to a certain level may be different. Furthermore, although total pressure
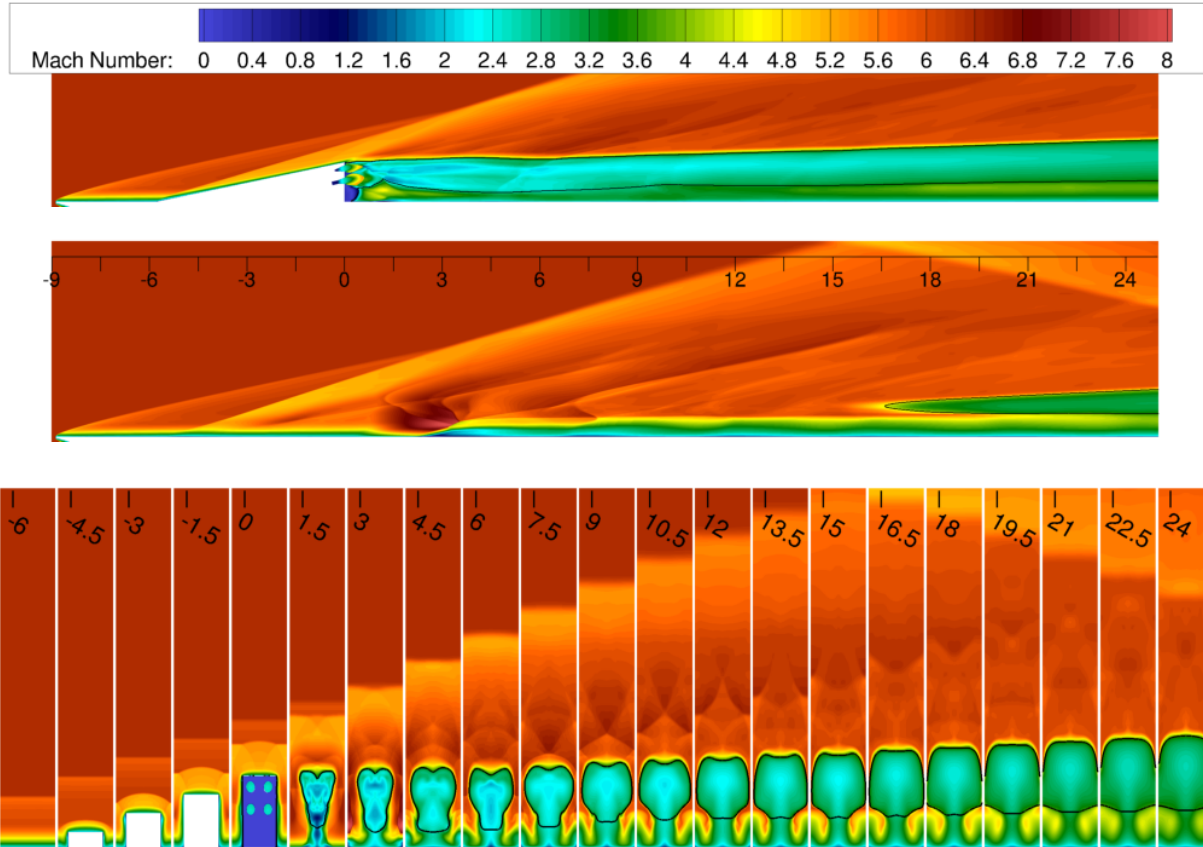
Figure 22: Contours of the Mach number on the z-planes obtained through the center of the injector ports, and half-way between the injectors, and x-planes at various downstream locations for the ramp injector simulations for case PoF/ToF/H2/R. Downstream distance is in inches. Black lines denotes the stoichiometric value of the inert species mass fraction.

losses directly correlate with the entropy gains for adiabatic systems, wall cooling can increase the total pressure. The PoG/ToG/He case used an adiabatic wall for the flat plate, whereas the PoF/ToF/H2 case used a cold wall. Therefore, it is also possible that the confluence of the mixing rates, and the differences in the flat plate cooling rates for the two cases lead to the unintuitive result. However, under most circumstances, the generalization that mixing increases with a corresponding decrease in the total pressure recovery is reasonable, and can be a useful engineering approximation.

The specific thrust potential is obtained by normalizing the thrust potential by the mass flow rate of air. The thrust potential for the "cold" case, PoG/ToG/He, is not shown because its value is significantly lower from the high total enthalpy cases, but thrust potential trends for the PoG/ToG/He case are consistent with those shown in the plots. Despite the relatively small decrease of only a 2-3% percentage points in the value of the total pressure recovery, the majority of the potential thrust is lost due to the shock wave induced by the leading edge of the plate. This is evident by the rapid drop in the values of the specific thrust potential just downstream from the inflow and shown in Figs. 23 and 24, for the strut and ramp injectors, respectively. Only a small fraction of the potential thrust is lost through the viscous and shock losses incurred on the injector bodies, except for the PoG/ToF/He case for the strut injector, which exhibits injector body-side separation, which causes additional losses. Just downstream of the injection plane, the thrust potential is augmented by the thrust produced by the downstream-oriented fuel injector ports. The amount of the augmenting thrust varies among the cases because, first, the value of the total temperature of the fuel
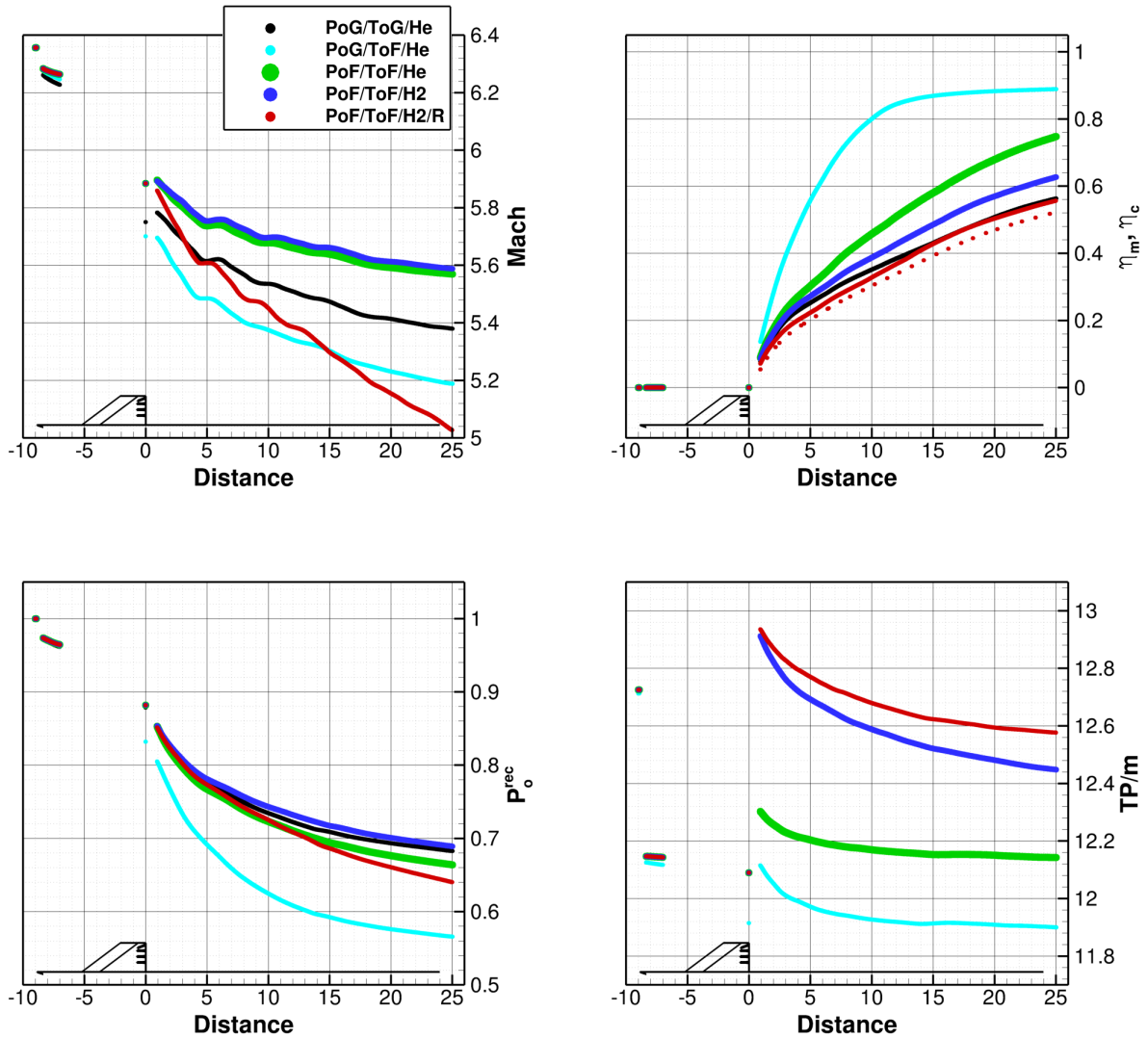
Figure 23: one-dimensional values of the Mach number, mixing and combustion (dotted) efficiencies, total pressure recovery, and the specific thrust potential (kN/(kg/s)) vs. the downstream distance (in inches) obtained from the simulations on the fine grid for the strut injector.

differs for case PoG/ToF/He from that of the other cases (see Table 3); second, the molecular weight of the fuel decreases from that of helium for the PoF/ToF/He case to that of hydrogen for the PoF/ToF/H2 case. Even though the fuel mass flow rate and the total temperature are the same for the helium and hydrogen cases, the decrease in the molecular weight of the fuel causes a corresponding increase in the value of the total pressure required to drive the desired mass through the fuel ports, thereby also increasing its thrust. Unlike the total pressure recovery, the value of the thrust potential increases when heat is released into the flow by combustion. This feature makes the thrust potential a good metric of losses that are important to the engine performance, i.e., viscous and shock losses cause a decrement to the thrust potential whereas heat release and axial fuel injection cause an augmentation. Interesting to also note is the relative importance of the axially-directed fuel ports, which at least for the case of hydrogen fuel, recover the thrust potential losses caused by the leading edge shock wave. This increase occurs despite the fact that the mass flow rate of the fuel is a small fraction (0.0292) of that of the incoming air. Another notable observation is the fact that the
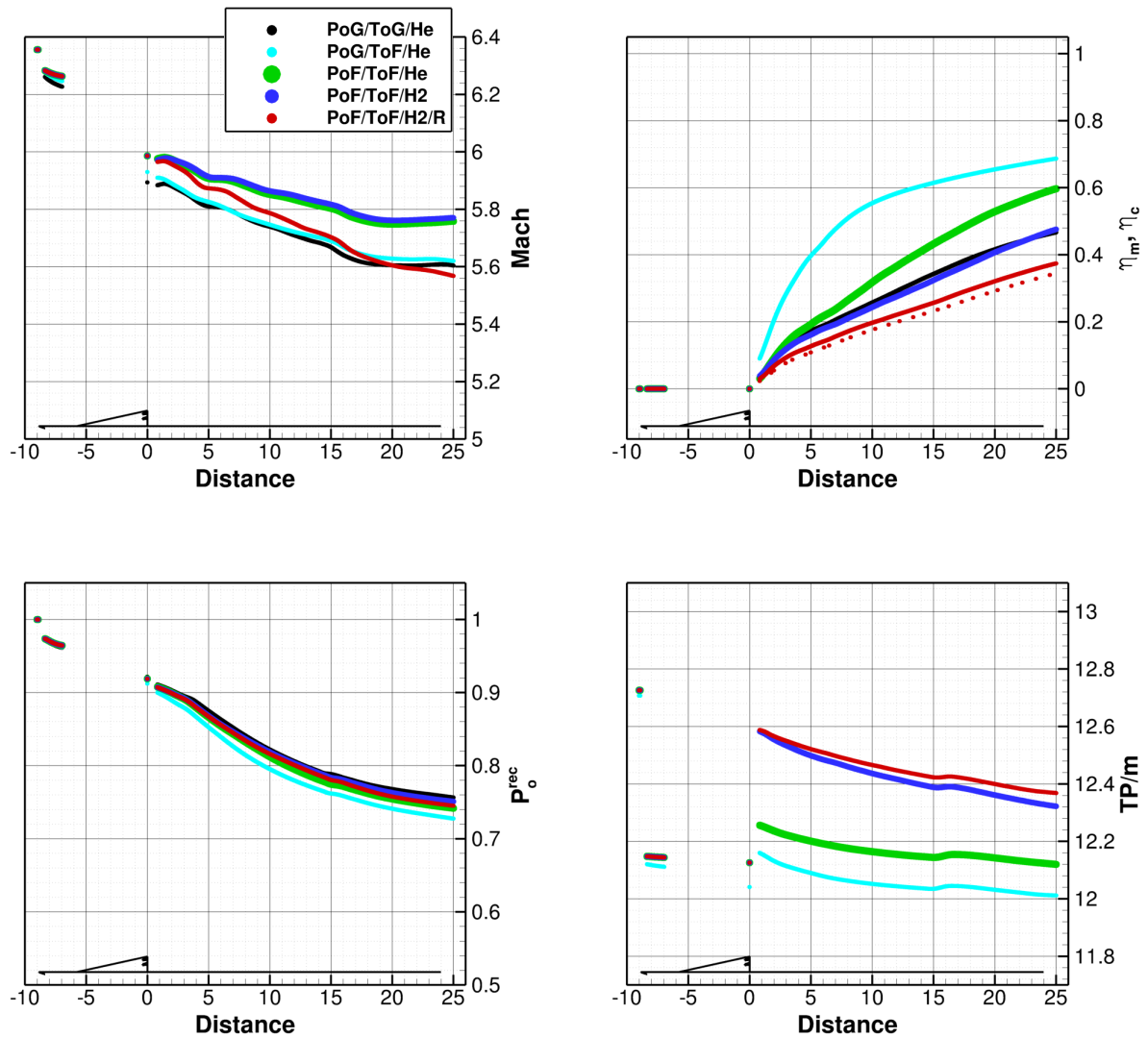
Figure 24: one-dimensional values of the Mach number, mixing and combustion (dotted) efficiencies, total pressure recovery, and the specific thrust potential (kN/(kg/s)) vs. the downstream distance (in inches) obtained from the simulations on the fine grid for the ramp injector.

thrust potential enhancement due to chemical heat release is a small fraction of the augmentation caused by the axially-injected fuel in as much as the current (open plate) injection configuration would produce the most thrust if the flowpath was simply truncated at the injection plane. However, the current result should be kept in perspective and should not be extrapolated to all flowpaths at hypervelocity flow conditions because the open plate configurations in the current simulations are not representative of properly designed and optimized propulsive flowpaths. In other words, the objectives of the EIMP experiments are only intended to investigate the fundamental aspects of mixing and losses under hypervelocity conditions.

Figure 25 shows a plot of total pressure recovery versus the mixing efficiency. For the strut injector, the amount of total pressure loss per unit mixing is about the same for all the cases, except the reacting one, which incurs Rayleigh losses in addition to the mixing losses. This plot indicates that the strut injector is equally efficient at mixing fuel-and-air regardless of the flow conditions. Furthermore, the slope of these
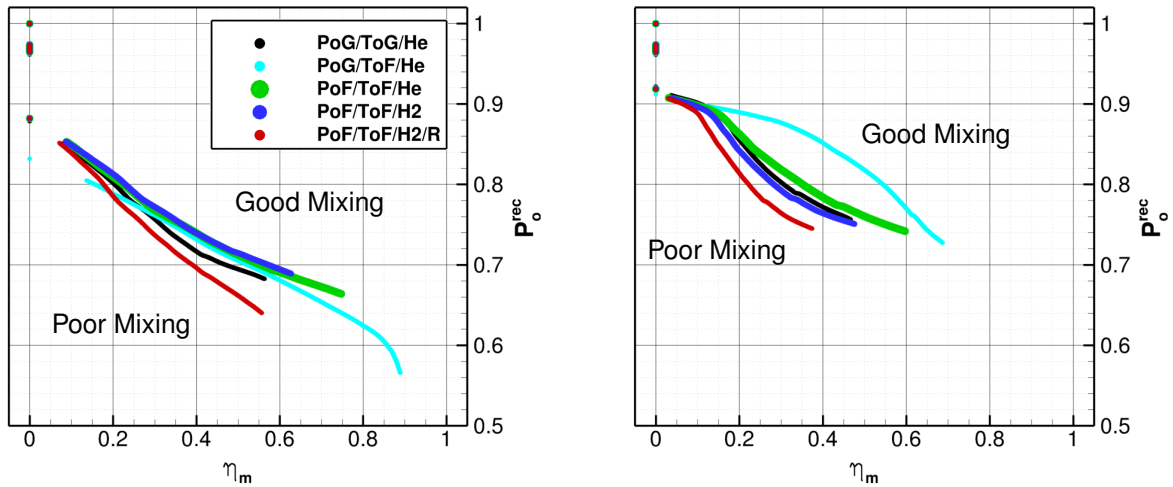
Figure 25: one-dimensional values of the total pressure recovery vs. mixing efficiency obtained from the simulations on the fine grid for the strut (left) and ramp (right) injectors.

curves is almost linear and could potentially be used to estimate losses from the mixing efficiency and vice versa. This could be useful if only one of the quantities could be obtained experimentally. For example, in the EIMP experiments gas sampling provides a measure of mixing, whereas the total pressure can not be accurately computed. Unfortunately, the same plot corresponding to the ramp injector does not collapse onto a line. This is not unexpected because, as discussed previously, the strength of the large-scale vortical motions induced by the ramp body, and therefore mixing performance, depend on the flow conditions. Nevertheless, the computational profile of this curve, computed at the relevant experimental conditions, could still serve as a tool to obtain total pressure recovery from the measured mixing efficiency. The most interesting profile is that for the PoG/ToF/He case. For that case, the ramp injector, unlike the strut injector, appears to be significantly more efficient at inducing mixing in the near-field of the injection plane. Despite this early efficiency, as the flow continues to mix, even this curve approaches those corresponding to the other cases. It would be important to further understand why and how this specific case departs from the general trend to determine whether these effects can be extended and used to reduce the level of the total pressure losses. Examining this simulation reveals that, not only the velocity difference parameter and the density ratios are the largest, but also the static and dynamic pressure ratios are the lowest as compared to the other cases. The value of the static pressure ratio corresponds to the only one (among both strut and ramp cases) that is significantly lower than one, indicating over- instead of under-expansion of the fuel plumes. The value of the dynamic pressure ratio is also the lowest among the cases, which suggests reduced penetration of the fuel plumes into the flow domain. These effects, when considered with the relatively large bluff body region created in the wake of the ramp, may suggest that a comparatively larger portion of the fuel is recirculated just downstream of the ramp, which would increase the fuel residence time and thereby enhance mixing. Overall, the ramp injector body and its downstream mixing field induce somewhat less total pressure loss than those for the strut. However, the amount of mixing induced at a given downstream distance is also lower than that for the strut. Such trade-offs, when considered together with the other metrics, such as the thrust potential, make comparisons between the different injectors quite complicated, and ultimately may prove that such comparisons are futile on the open plate configuration without further considering a ducted flowpath, that includes space-filling injector arrangements, together with the knowledge of the specific flight trajectory.

SUMMARY AND CONCLUSIONS

Ground based experimentation at hypervelocity conditions presents an economical and technical challenge. The current work utilizes Reynolds Averaged Simulations (RAS) to demonstrate that it is possible to utilize the "cold" flow conditions defined for the Enhanced Injection and Mixing Project (EIMP) with helium as a fuel simulant to effectively model fuel injection, mixing, and the corresponding total pressure losses that would occur, under hypervelocity flight conditions. For the purpose of the demonstration, five cases, and two different injector geometries, are investigated with the flow conditions that match the Mach number to that expected at the combustor entrance in flight. The total enthalpy and total pressure were then varied to systematically transition the EIMP simulated ground test conditions to those expected in flight. The first case used a set of flow conditions that will be used as the baseline for the EIMP experiments in the Arc-Heated Scramjet Test Facility (AHSTF), and consists of the "cold" (low total enthalpy) flow under facility-limited total pressure conditions with helium as a simulant for the hydrogen fuel. The second case maintained the value of the total pressure and continued to utilize helium, but with the value of the total enthalpy corresponding to that expected in flight. The remaining three cases were for flow conditions at true flight total enthalpy and total pressure conditions. The first two of these three cases illustrated the impact of the fuel simulant on mixing and losses by using helium and hydrogen (non-reacting) gases, respectively. The final case investigated the impact of heat release by allowing chemical reactions to take place. The two injectors used are a fuel-placement device based on a slender, swept, strut protruding into the core of the flowpath, and a large vortex generator based on an unswept ramp. This choice represents two main categories of injectors typically considered in the propulsive devices used for high-speed flight. The contours of the Mach number obtained from the RAS revealed that qualitatively the flow fields for all the cases utilizing the same injector are similar. The one-dimensional values of the mass-flux-weighted average Mach number, mixing and combustion efficiencies, total pressure recovery, and specific thrust potential were used to quantify the differences among the cases and injectors. It was found that the case corresponding to the conditions utilizing the true flight enthalpy but with ground-based facility total pressure, and using helium as a fuel simulant, produced results that were furthest removed from those obtained for the true flight conditions with hydrogen as a fuel. However, the baseline case corresponding to the ground-based "cold" flow conditions (i.e., the first case) and utilizing helium as a fuel simulant was able to closely reproduce both the mixing and total pressure losses corresponding to cases with the true hypervelocity flight conditions with both non-reacting and reacting hydrogen fuel. These findings suggest that "cold" flow experiments using helium as a substitute for hydrogen are a valid means to reproduce the mixing characteristics of hypervelocity scramjets. Further understanding of the competing factors that lead to this result are left for future work.

FUTURE WORK

There are several near and long term future goals for the CFD analysis of the EIMP. In the near term, as the EIMP experimental data become available, RAS simulations will be rerun at the exact conditions of the experiment. The modeling constants, such as the turbulent Schmidt number, will be calibrated to best match the experimental data, primarily the gas sampled mole fractions of the fuel simulant. These calibrated simulations will then be further processed to gain insight into the flow structure and flow physics generated by the various injectors and to extract both plume characteristics and mixing metrics. Additionally, once the CFD is reasonably calibrated, the simulations can be further used to explore the relationships between mixing performance and losses that depend on both the flow and geometrical considerations.

In the longer term, the CFD will be coupled with optimization software (e.g., DAKOTA[33]) to optimize injector configurations based on maximizing the rate of mixing while simultaneously minimizing losses based on either total pressure recovery or the thrust potential metrics. This approach is expected to "drive" configurations to those with minimum pressure loss for a desired amount of mixing. One quantity to optimize, for example, will be the distance between adjacent injectors in an array across a Mach number range. Such optimized injectors will be further evaluated in a ducted, instead of an open flowpath.

Most computations will utilize RAS, however, several LES computations will also be used to further validate RAS, and investigate the details of the unsteady flow features. Validating RAS via LES is of interest because the available experimental data sets are typically sparse. Furthermore, LES is expected to be more accurate then RAS in flows with multiscale, geometry-induced, strong vortical flows with recirculation zones and flow separation. LES will also be utilized for injection cases explicitly utilizing unsteady effects, such as for cases of pulsed fuel injection.

ACKNOWLEDGMENTS

REFERENCES

[1] Drozda, T. G., Axdahl, E. L., and Cabell, K. F., **Pre-Test CFD for the Design and Execution of the Enhanced Injection and Mixing Project at NASA Langley Research Center**, in *JANNAF 46th CS / 34th APS / 34th EPSS / 28th PSHS Joint Subcommittee Meeting*, Albuquerque, NM (Dec. 2014).

[2] Baurle, R., **Analysis of Facility Non-Equilibrium Thermodynamic Effects on HIFiRE Ground Tests**, in *JANNAF 46th CS / 34th APS / 34th EPSS / 28th PSHS Joint Subcommittee Meeting*, Albuquerque, NM (Dec. 2014).

[3] Papamoschou, D. and Roshko, A., **The Compressible Turbulent Shear Layer: An Experimental Study**, J. Fluid Mech., 197:453–477 (1988).

[4] Givi, P., Madnia, C. K., Steinberger, C. J., Carpenter, M. H., and Drummond, J. P., **Effects of Compressibility and Heat Release in a High Speed Reacting Mixing Layer**, Combust. Sci. Technol., 78:33–68 (1991).

[5] Drummond, J. P. and Givi, P., **Suppression and Enhancement of Mixing in High-Speed Reacting Flow Fields**, in J. D. Buckmaster, T. L. Jackson, and A. Kumar, editors, *Combustion in High-Speed Flows*, pages 191–229, Kluwer Academic Publishers, Netherlands (1994).

[6] Vreman, A. W., Sandham, N. D., and Luo, K. H., **Compressible Mixing Layer Growth Rate and Turbulence Characteristics**, J. Fluid Mech., 320:235–258 (7 1996).

[7] Foysi, H. and Sarkar, S., **The Compressible Mixing Layer: An LES Study**, Theor. Comp. Fluid. Dyn., 24:565–588 (2010).

[8] Drummond, J. P., Carpenter, M. H., and Riggins, D. W., **Mixing and Mixing Enhancement in Supersonic Reacting Flow Fields**, in S. N. B. Murthy and E. T. Curran, editors, *High Speed Propulsion Systems*, vol. 137 of *AIAA Progress Series*, chap. 7, pages 383–455, American Institute of Aeronautics and Astronautics (1991).

[9] Lee, J., Lin, K.-C., and Eklund, D., **Challenges in Fuel Injection for High-Speed Propulsion Systems**, AIAA J., 53(6):1405–1423 (Jun. 2015).

[10] Cabell, K., Drozda, T. G., Axdahl, E. L., and Danehy, P. M., **The Enhanced Injection and Mixing Project at NASA Langley**, in *JANNAF 46th CS / 34th APS / 34th EPSS / 28th PSHS Joint Subcommittee Meeting*, Albuquerque, NM (Dec. 2014).

[11] McClinton, C. R., ***Evaluation of Scramjet Combustor Performance Using Cold Nonreactive Mixing Tests***, in *14th AIAA Aerospace Sciences Meeting*, Washington, DC (Jan. 1976).

[12] Mao, M., Riggins, D. W., and McClinton, C. R., ***Numerical Simulation of Transverse Fuel Injection***, in *Computational Fluid Dynamics Symposium on Aeropropulsion*, NASA-CP-3078, pages 635–667, NASA, Cleveland, OH (Apr. 1990).

[13] Baurle, R. A., Fuller, R. P., White, J. A., Chen, T. H., Gruber, M. R., and Nejad, A. S., ***An Investigation of Advanced Fuel Injection Schemes for Scramjet Combustion***, in *36th Aerospace Sciences Meeting and Exhibit*, Reno, NV (Jan. 1998).

[14] Cabell, K. F. and Rock, K. E., ***A Finite Rate Chemical Analysis of Nitric Oxide Flow Contamination Effects on Scramjet Performance***, Tech. Rep. TP-212159, NASA (2003).

[15] Kidd III, F. G., Narayanaswamy, V., Danehy, P. M., Inman, J. A., Bathel, B. F., Cabell, K. F., Hass, N. E., Capriotti, D. P., Drozda, T. G., and Johansen, C. T., ***Characterization of the NASA Langley Arc Heated Scramjet Test Facility Using NO PLIF***, in *30th AIAA Aerodynamic Measurement Technology and Ground Testing Conference*, Atlanta, GA (Jun. 2014).

[16] Heiser, W. H. and Pratt, D. T., ***Hypersonic Airbreathing Propulsion***, AIAA, Washington, DC (1994).

[17] Public Domain Aeronautical Software (PDAS), ***Properties of the U.S. Standard Atmosphere 1976***, http://www.pdas.com/atmos.html (Apr. 2016).

[18] Magnussen, B. F. and Hjertager, B. H., ***On Mathematical Modeling of Turbulent Combustion with Special Emphasis on Soot Formation and Combustion***, in *Sixteenth Symposium (International) on Combustion*, pages 719–729 (1976).

[19] Marinov, N. M., Westbrook, C. K., and Pitz, W. J., ***Detailed and Global Chemical Kinetics Model for Hydrogen***, in S. H. Chan, editor, *Transport Phenomena in Combustion*, Proceedings of the Eigth International Symposium on Transport Phenomena in Combustion, pages 118–129 (Jul. 1995).

[20] Brown, G. L. and Roshko, A., ***On Density Effects and Large Structure in Turbulent Mixing Layers***, J. Fluid Mech., 64:775–816 (1974).

[21] Bogdanoff, D. W., ***Compressibility Effects in Turbulent Shear Layers***, AIAA J., 21(6):926–927 (1983).

[22] Riggins, D. W., McClinton, C. R., and Vitt, P. H., ***Thrust Losses in Hypersonic Engines Part 1: Methodology***, J. Propul. Power., 13(2):281–287 (1997).

[23] VULCAN-CFD, ***http://vulcan-cfd.larc.nasa.gov/*** (Apr. 2016).

[24] van Leer, B., ***Towards the Ultimate Conservative Difference Scheme. V: A Second-Order Sequel to Godunov's Method***, J. Comput. Phys., 32(1):101–136 (Jul. 1979).

[25] Edwards, J. R., ***A Low-Diffusion Flux-Splitting Scheme for Navier-Stokes Calculations***, Comput. Fluids., 26(6):635–659 (Jul. 1997).

[26] McBride, B. J., Gordon, S., and Reno, M. A., ***Thermodynamic Data for Fifty Reference Elements***, NASA Technical Paper 3287/REV1, NASA, Cleveland, OH (Feb. 2001).

[27] Pulliam, T. H. and Chaussee, D. S., ***A Diagonal Form of an Implicit Approximate-Factorization Algorithm***, J. Comput. Phys., 39(2):347–363 (Feb. 1981).

[28] Menter, F. R., ***Two-Equation Eddy-Viscosity Turbulence Models for Engineering Applications***, AIAA J., 32(8):1598–1605 (Aug. 1994).

[29] Wilcox, D. C., ***Turbulence Modeling for CFD***, DCW Industries, Inc., La Cañada, CA (2000).

[30] Roache, P. J., ***Verification and Validation in Computational Science and Engineering***, Hermosa Publishers (1998).

[31] Schlichting, H., ***Boundary-Layer Theory***, McGraw-Hill Book Co., New York, NY, seventh edn. (1979).

[32] Hussain, A. K. M. F. and Husain, Z. D., ***Turbulence Structure in the Axisymmetric Free Mixing Layer***, AIAA J., 18(12):1462–1469 (Dec. 1980).

[33] Adams, B., Bohnhoff, W., Dalbey, K., Eddy, J., Eldred, M., Gay, D., Haskell, K., Hough, P., and Swiler, L., ***DAKOTA, A Multilevel Parallel Object-Oriented Framework for Design Optimization, Parameter Estimation, Uncertainty Quantification, and Sensitivity Analysis: Version 5.0 User's Manual***, Sandia Technical Report SAND2010-2184, Sandia (May 2013).